



Spectroscopy[®]

Solutions for Materials Analysis

October 2017 Volume 32 Number 10

www.spectroscopyonline.com

**Lead in Our
Food Supply**

**ICP-OES Analysis of
Rare Earth Elements**

**Tumor Sample Analysis
with Tandem LA-LIBS
Coupled to ICP-MS**

**Calibration Transfer
Chemometrics**



UBM

GET **MORE** SPECTRAL DATA IN LESS TIME

The Ocean FX Spectrometer Offers Fast Acquisition Speed, Robust Communications and Onboard Processing



4,500
SCANS PER SECOND!

HIGH-SPEED ACQUISITION

Acquire and process more spectral data in less time

Measures flicker and fast color cycling in lighting

ONBOARD PROCESSING

Improve SNR, reduce data transfer time and store up to 50,000 spectra

Has onboard scan averaging to speed up processing time

ROBUST INTERFACE

Operates via Gigabit Ethernet, Wi-Fi, SPI and USB

Ideal for remote sensing and handheld monitoring



info@oceanoptics.com • www.oceanoptics.com • **US** +1 727-733-2447
EUROPE +31 26-3190500 • **ASIA** +86 21-6295-6600

Brains + Brawn



Powered by **milestone connect**

Highest throughput rotors

No method development

Remote system control

Enhanced safety features

Meet the new Milestone Ethos UP, the world's most intelligent microwave digestion system.

When it comes to rotor-based microwave sample prep, nothing comes close to the new Milestone Ethos UP. With over 300 pre-set digestion methods built right in, our exclusive **EasyControl software** is the smart approach to microwave digestion. Plus, new **Milestone Connect** offers remote system control, 24/7 technical support and direct access to a comprehensive library of content developed especially for lab professionals.

Need more? The Milestone Ethos UP isn't just intelligent, it's the most powerful microwave digestion system on the market today. Featuring the highest throughput rotors, stainless steel construction and patented vent-and-reseal technology, the Ethos UP ensures market-leading safety and productivity. Very smart.

See how Ethos UP's brains + brawn can help you work smarter.
Go to www.milestonesci.com/smart.



Ethos UP



UltraWAVE



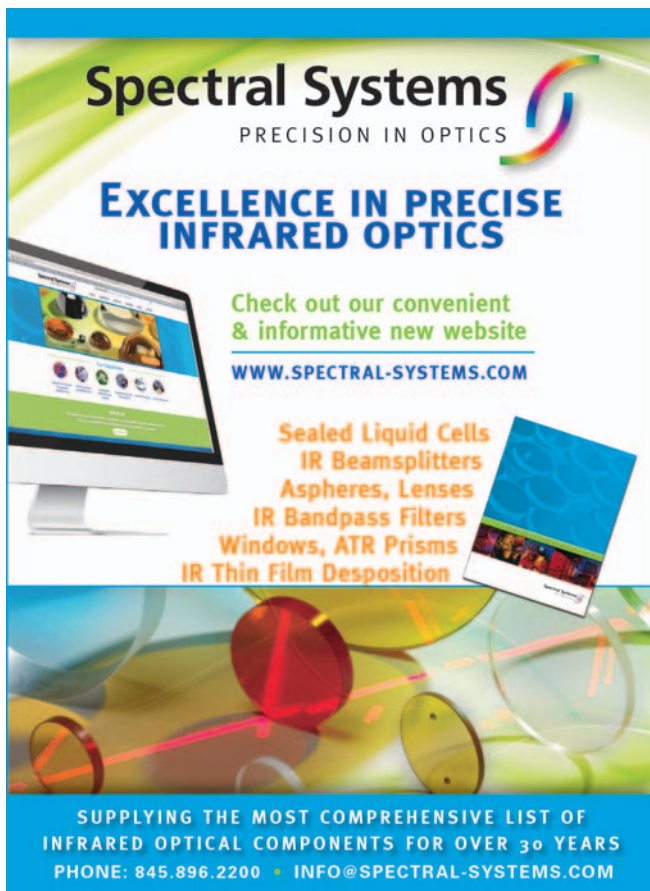
UltraCLAVE

Microwave Digestion

Mercury | Clean Chemistry | Ashing | Extraction | Synthesis

milestonesci.com | 866.995.5100





Spectral Systems
PRECISION IN OPTICS

EXCELLENCE IN PRECISE INFRARED OPTICS

Check out our convenient & informative new website
WWW.SPECTRAL-SYSTEMS.COM

Sealed Liquid Cells
IR Beamsplitters
Aspheres, Lenses
IR Bandpass Filters
Windows, ATR Prisms
IR Thin Film Deposition

SUPPLYING THE MOST COMPREHENSIVE LIST OF INFRARED OPTICAL COMPONENTS FOR OVER 30 YEARS
PHONE: 845.896.2200 • INFO@SPECTRAL-SYSTEMS.COM

Spectroscopy®

MANUSCRIPTS: To discuss possible article topics or obtain manuscript preparation guidelines, contact the editorial director at: (732) 346-3020, e-mail: Laura.Bush@ubm.com. Publishers assume no responsibility for safety of artwork, photographs, or manuscripts. Every caution is taken to ensure accuracy, but publishers cannot accept responsibility for the information supplied herein or for any opinion expressed.

SUBSCRIPTIONS: For subscription information: *Spectroscopy*, P.O. Box 6196, Duluth, MN 55806-6196; (888) 527-7008, 7:00 a.m. to 6:00 p.m. CST. Outside the U.S., +1-218-740-6477. Delivery of *Spectroscopy* outside the U.S. is 3–14 days after printing. Single-copy price: U.S., \$10.00 + \$7.00 postage and handling (\$17.00 total); Canada and Mexico, \$12.00 + \$7.00 postage and handling (\$19.00 total); Other international, \$15.00 + \$7.00 postage and handling (\$22.00 total).

CHANGE OF ADDRESS: Send change of address to *Spectroscopy*, P.O. Box 6196, Duluth, MN 55806-6196; provide old mailing label as well as new address; include ZIP or postal code. Allow 4–6 weeks for change. Alternately, go to the following URL for address changes or subscription renewal: <http://ubmsubs.ubm.com/?pubid=SPEC>

RETURN ALL UNDELIVERABLE CANADIAN ADDRESSES TO: IMEX Global Solutions, P.O. Box 25542, London, ON N6C 6B2, CANADA. PUBLICATIONS MAIL AGREEMENT No.40612608.

REPRINT SERVICES: Reprints of all articles in this issue and past issues are available (500 minimum). Call 877-652-5295 ext. 121 or e-mail bkolb@wrightsmedia.com.

com. Outside US, UK, direct dial: 281-419-5725. Ext. 121

C.A.S.T. DATA AND LIST INFORMATION: Contact Melissa Stillwell, (218) 740-6831; e-mail: Melissa.Stillwell@ubm.com

INTERNATIONAL LICENSING: Maureen Cannon, (440) 891-2742, fax: (440) 891-2650; e-mail: Maureen.Cannon@ubm.com



Starna

ISO/IEC 17025 & ISO Guide 34 Accredited
Simple UV/VIS/NIR Validation
Permanently sealed cells for repeat use
Absorbance, Stray Light,
Wavelength, Resolution
NIST Traceable

Certified Reference Materials

NEW USP 857 REFERENCES

Starna Cells, Inc.
PO Box 1919 Atascadero, CA 93423
Phone: (800) 228-4482 USA or (805) 466-8855 outside USA
sales@starnacells.com www.starnacells.com



© 2017 UBM. All rights reserved. No part of this publication may be reproduced or transmitted in any form or by any means, electronic or mechanical including by photocopy, recording, or information storage and retrieval without permission in writing from the publisher. Authorization to photocopy items for internal/educational or personal use, or the internal/educational or personal use of specific clients is granted by UBM for libraries and other users registered with the Copyright Clearance Center, 222 Rosewood Dr. Danvers, MA 01923, 978-750-8400 fax 978-646-8700 or visit <http://www.copyright.com> online. For uses beyond those listed above, please direct your written request to Permission Dept. fax 440-756-5255 or email: Maureen.Cannon@ubm.com.

UBM Americas provides certain customer contact data (such as customers' names, addresses, phone numbers, and e-mail addresses) to third parties who wish to promote relevant products, services, and other opportunities that may be of interest to you. If you do not want UBM Americas to make your contact information available to third parties for marketing purposes, simply call toll-free 866-529-2922 between the hours of 7:30 a.m. and 5 p.m. CST and a customer service representative will assist you in removing your name from UBM Americas lists. Outside the U.S., please phone 218-740-6477.

Spectroscopy does not verify any claims or other information appearing in any of the advertisements contained in the publication, and cannot take responsibility for any losses or other damages incurred by readers in reliance of such content.

Spectroscopy welcomes unsolicited articles, manuscripts, photographs, illustrations and other materials but cannot be held responsible for their safekeeping or return.

To subscribe, call toll-free 888-527-7008. Outside the U.S. call 218-740-6477.

UBM Americas (www.ubmamericas.com) is a leading worldwide media company providing integrated marketing solutions for the Fashion, Life Sciences and Powersports industries. UBM Americas serves business professionals and consumers in these industries with its portfolio of 91 events, 67 publications and directories, 150 electronic publications and Web sites, as well as educational and direct marketing products and services. Market leading brands and a commitment to delivering innovative, quality products and services enables UBM Americas to "Connect Our Customers With Theirs." UBM Americas has approximately 1000 employees and currently operates from multiple offices in North America and Europe.



Maximizing the return-on-investment for the refining & petrochemical industries

TALYS ASP400

TALYS ASP400 series is a single-point fiber optics based industrial FT-NIR analyzer designed to make in-line monitoring and control of continuous processes easy. Its simple installation enables real-time process monitoring, determination of stream properties or physical qualities, process characterization and early troubleshooting. The embedded controller provides full connectivity to DCS: Modbus TCP/IP, and OPC. With virtually no scheduled maintenance for 5-years, it delivers a low total cost of ownership. Learn more at abb.com/analytical or contact us at ftir@ca.abb.com



HITACHI
Inspire the Next

Hitachi provides comprehensive laboratory solutions, serving your needs inside AND outside the lab.

Contact us about our Fall Specials!

Think Outside the Lab

Spectroscopy X-ray Fluorescence Thermal Analysis

Hitachi High-Technologies Science America, Inc.
www.hitachi-hightech.com Tel. 1-800-548-9001

NeoSpectra
MicroDevelopment Kit

The NeoSpectra Micro is a revolutionary chip-sized FT-IR spectrometer with a spectral range of 1,250 - 2,500 nm. It is accurate, cost-effective, and ubiquitous across many different applications. The NeoSpectra Micro Development Kit incorporates the Micro onto an SPI Development Board, allowing our customers to have a plug-and-play solution for replicating the typical performance of the NeoSpectra Micro. **Begin developing your unique platform today!**

What's included:

- NeoSpectra Micro Development Board with SPI Interface
- Raspberry Pi Board
- Micro SD Card
- Mini HDMI Cable
- Micro USB Cable



Please visit our website www.neospectra.com/shop-product to purchase yours today, or email info@si-ware.com for more information.

Spectroscopy®

485F US Highway One South, Suite 210
Iselin, NJ 08830
(732) 596-0276
Fax: (732) 647-1235

Michael J. Tessalone
Vice President/Group Publisher
Michael.Tessalone@ubm.com

Stephanie Shaffer
Publisher
Stephanie.Shaffer@ubm.com

Edward Fantuzzi
Associate Publisher
Edward.Fantuzzi@ubm.com

Michael Kushner
Senior Director, Digital Media
Michael.Kushner@ubm.com

Laura Bush
Editorial Director
Laura.Bush@ubm.com

Megan L'Heureux
Managing Editor
Meg.L'Heureux@ubm.com

Stephen A. Brown
Group Technical Editor
Stephen.Brown@ubm.com

Cindy Delonas
Associate Editor
Cindy.Delonas@ubm.com

Kristen Moore
Webcast Operations Manager
Kristen.Moore@ubm.com

Vania Oliveira
Project Manager
Vania.Oliveira@ubm.com

Sabina Advani
Digital Production Manager
Sabina.Advani@ubm.com

Kaylynn Chiarello-Ebner
Managing Editor, Special Projects
Kaylynn.Chiarello.Ebner@ubm.com

Dan Ward
Art Director
dward@hcl.com

Anne Lavigne
Marketing Manager
Anne.Lavigne@ubm.com

Melissa Stillwell
C.A.S.T. Data and List Information
Melissa.Stillwell@ubm.com

Wright's Media
Reprints
bkolb@wrightsmedia.com

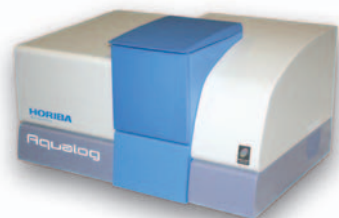
Maureen Cannon
Permissions
Maureen.Cannon@ubm.com

Jesse Singer
Production Manager
jsinger@hcl.com

Wendy Bong
Audience Development Manager
Wendy.Bong@ubm.com

Ross Burns
Audience Development Assistant Manager
Ross.Burns@ubm.com

A-TEEM™ Molecular Fingerprinting



The Future of Fluorescence...

There's more to colored molecules than meets the eye. Many applications require quantification of individual organic compounds in complex mixtures. Traditional methods for these measurements are HPLC, GC-MS, UV-Vis...But now measurements that took a half hour to a day can be done in minutes with Excitation-Emission Matrix (EEM).

HORIBA has combined an ultrafast CCD that's up to 4,000 times faster than traditional PMT-based fluorometers, with a new, patented A-TEEM™ technology in our Aqualog® that uses the absorbance, transmittance and EEM data to fingerprint molecules with high specificity and ultrahigh-sensitivity at a 6 million nm/min emission scan rate! A-TEEM can easily and effectively identify, quantify and understand dynamics of molecules in mixtures, under a variety of conditions...

in the blink of an eye.

See it for yourself at www.aqualog.com. **But don't blink, or you'll miss it!**

horiba.com/scientific

email: info.sci@horiba.com



Spectroscopy

October 2017

Volume 32 Number 10



Cover image courtesy of
taboga/Shutterstock.

ON THE WEB

WEB SEMINARS

A-TEEM Molecular Fingerprinting: A New and Exciting Spectroscopy Technique

Dr. Adam Gilmore, Horiba Scientific

Improving Extractables and Leachables and Trace Metal Testing of Pharmaceutical Packaging

Dr. Mark Jordi and Dr. James Woods, Jordi Labs and Laura Thompson, Milestone Inc.

Single Particle Mode or Hyphenated ICP-MS? A Discussion of Nanoparticle Analysis in Complex Matrices

Dr. Susana Cuello Nuñez, LGC Limited, and Steve Wilbur, Agilent Technologies

How to Maximize Your ICP-MS Performance

Dr. Daniel Kutscher and Dr. Dhinesh Asogan, Thermo Fisher Scientific

[spectroscopyonline.com/SpecWebSeminars](http://www.spectroscopyonline.com/SpecWebSeminars)

Like *Spectroscopy* on Facebook:
www.facebook.com/SpectroscopyMagazine



Follow *Spectroscopy* on Twitter:
<https://twitter.com/spectroscopyMag>



Join the *Spectroscopy* Group on LinkedIn
<http://linkd.in/SpecGroup>



CONTENTS

COLUMNS

Atomic Perspectives 12

Our Daily Dose of Poison: A Look at Lead in the Food Supply

Patricia Atkins

How much lead is in our daily lives? We take a look at current research concerning lead in the United States food supply and investigations using ICP-MS into the measurement of high concentrations of lead in food.

Chemometrics in Spectroscopy 18

Calibration Transfer Chemometrics, Part I: Review of the Subject

Jerome Workman, Jr., and Howard Mark

Calibration transfer involves multiple strategies and mathematical techniques for applying a single calibration database to two or more instruments. Here, we explain the methods to modify the spectra or regression vectors to correct differences between instruments.

Lasers and Optics Interface 26

Combining Broadband Spectra and Machine Learning to Derive Material Properties

Steve Buckley

With methods such as infrared, Raman, and LIBS, the spectral background contains a wealth of information about material properties of the sample. Now, such information can be derived by artificial intelligence and machine learning algorithms.

PEER-REVIEWED ARTICLES

Determination of Rare Earth Elements in Geological and Agricultural Samples by ICP-OES 32

Clarice D. B. Amaral, Raquel C. Machado, Juan A. V. A. Barros,

Alex Virgilio, Daniela Schiavo, Ana Rita A. Nogueira, and Joaquim A. Nóbrega

This method demonstrates that ICP-OES is a suitable alternative to ICP-MS for the determination of rare earth elements in geological and agricultural samples.

Tandem LA-LIBS Coupled to ICP-MS for Comprehensive Analysis of Tumor Samples. 42

Maximilian Bonta, Szilvia Török, Balazs Döme, and Andreas Limbeck

This method demonstrates the excellent suitability of a multimodal approach that combines LA-ICP-MS with LIBS for the analysis of tumor samples, particularly when the standalone techniques cannot detect all the elements of interest.

FEATURE

Effective Removal of Isobaric Interferences on Strontium and Lead Using Triple-Quadrupole ICP-MS 38

Daniel Kutscher, Simon Lofthouse, Simon Nelms, and Shona McSheehy Ducos

Unresolved interferences can lead to biased results in ICP-MS analyses. Here we describe an approach for removing those interferences using reactive gases.

DEPARTMENTS

News Spectrum.	10
Products & Resources.	47
Ad Index.	49

Spectroscopy (ISSN 0887-6703 [print], ISSN 1939-1900 [digital]) is published monthly by UBM LLC 131 West First Street, Duluth, MN 55802-2065. *Spectroscopy* is distributed free of charge to users and specifiers of spectroscopic equipment in the United States. *Spectroscopy* is available on a paid subscription basis to nonqualified readers at the rate of: U.S. and possessions: 1 year (12 issues), \$74.95; 2 years (24 issues), \$134.50. Canada/Mexico: 1 year, \$95; 2 years, \$150. International: 1 year (12 issues), \$140; 2 years (24 issues), \$250. Periodicals postage paid at Duluth, MN 55806 and at additional mailing offices. POSTMASTER: Send address changes to *Spectroscopy*, P.O. Box 6196, Duluth, MN 55806-6196. PUBLICATIONS MAIL AGREEMENT NO. 40612608, Return Undeliverable Canadian Addresses to: IMEX Global Solutions, P. O. Box 25542, London, ON N6C 6B2, CANADA. Canadian GST number: R-124213133RT001. Printed in the U.S.A.

Editorial Advisory Board

Fran Adar Horiba Scientific

Russ Algar University of British Columbia

Matthew J. Baker University of Strathclyde

Ramon M. Barnes University of Massachusetts

Matthieu Baudalet University of Central Florida

Rohit Bhargava University of Illinois at Urbana-Champaign

Paul N. Bourassa Blue Moon Inc.

Michael S. Bradley Thermo Fisher Scientific

Deborah Bradshaw Consultant

Lora L. Brehm The Dow Chemical Company

George Chan Lawrence Berkeley National Laboratory

David Lankin University of Illinois at Chicago,
College of Pharmacy

Barbara S. Larsen DuPont Central Research and Development

Bernhard Lendl Vienna University of Technology (TU Wien)

Ian R. Lewis Kaiser Optical Systems

Rachael R. Ogorzalek Loo University of California Los Angeles, David Geffen School of Medicine

Howard Mark Mark Electronics

R.D. McDowall McDowall Consulting

Gary McGeorge Bristol-Myers Squibb

Linda Baine McGown Rensselaer Polytechnic Institute

Francis M. Mirabella Jr. Mirabella Practical Consulting Solutions, Inc.

Ellen V. Miseo Illuminate

Michael L. Myrick University of South Carolina

John W. Olesik The Ohio State University

Steven Ray State University of New York at Buffalo

Jim Rydzak Specere Consulting


Jerome Workman Jr. Unity Scientific

Lu Yang National Research Council Canada

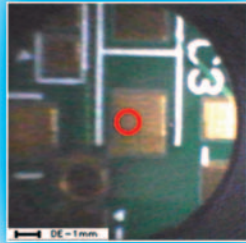
Spectroscopy's Editorial Advisory Board is a group of distinguished individuals assembled to help the publication fulfill its editorial mission to promote the effective use of spectroscopic technology as a practical research and measurement tool. With recognized expertise in a wide range of technique and application areas, board members perform a range of functions, such as reviewing manuscripts, suggesting authors and topics for coverage, and providing the editor with general direction and feedback. We are indebted to these scientists for their contributions to the publication and to the spectroscopy community as a whole.

NEW

SMALL SPOT ELEMENTAL ANALYSIS BY EDXRF




NEW



Automatic collimators
for 1, 3 or 10 mm
analysis areas


NEXDEVS

Analyze $_{11}\text{Na} - _{92}\text{U}$
non-destructively



Applied Rigaku Technologies, Inc.

website: www.RigakuEDXRF.com | email: info@RigakuEDXRF.com



News Spectrum

Spectroscopy Announces the Winner of the 2018 Emerging Leader in Atomic Spectroscopy Award

John M. Cottle, a professor of earth science at the University of California, Santa Barbara, has won the 2018 Emerging Leader in Atomic Spectroscopy Award, which is presented by *Spectroscopy* magazine. This annual award, begun in 2017, recognizes the achievements and aspirations of a talented young atomic spectroscopist, selected by an independent scientific committee.



John M. Cottle

The award will be presented to Cottle at the 2018 Winter Conference on Plasma Spectrochemistry, where he will give a plenary lecture.

Cottle is a leader in the development of novel laser-ablation inductively coupled plasma-mass spectrometry (LA-ICP-MS) measurements and their application to tectonic questions in convergent orogens. Whereas most pioneers of new MS techniques are laboratory based, and most workers at the forefront of tectonics are field based, Cottle combines both.

In particular, Cottle has pioneered three breakthrough measurement methods for geochemical data collection using

LA-ICP-MS. One is the development of single-pulse laser-ablation chronology for U-Pb and Th-Pb laser ablation, using a single laser pulse instead of the typical 80–200 pulses. This approach dramatically increases sample throughput, enabling very large numbers of grains to be dated, and it uses only ~1% of the mineral. The breakthrough behind this advance lies in integrating the entire transient peak, rather than measuring just peak height, thereby avoiding differential detector response. Cottle's groundbreaking paper describing this approach was awarded the New Wave Research Laser Ablation Prize for "the most original and novel work using laser ablation in analytical chemistry."

Subsequently, Cottle and colleagues have extended this method to single-pulse depth-profiling and three-dimensional mapping of zircon, monazite, titanite, and rutile. Conventional laser-ablation depth profiling is based on 20–30 s of continuous ablation, leading to smearing of the profile and an inability to precisely quantify steps or reversals in mineral zoning. Cottle's pioneering method provides two orders of magnitude increase in resolution by analyzing each 50–100 nm thick layer of crystal individually.

Cottle received his D.Phil. from the University of Oxford, UK, in 2008, following an M.Sc. and B.Sc. from the University of Otago, New Zealand. ■

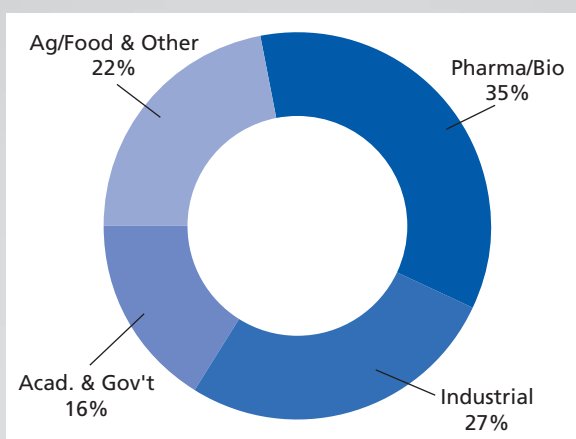
MARKET PROFILE: BENCHTOP NMR

Over the past decade, benchtop nuclear magnetic resonance (NMR) instruments have been used in the petroleum and petrochemical industries for process control applications. Increased use of the technology in the pharmaceutical, agriculture, and food industries during the last few years has prompted a surge in growth in the market for benchtop NMR systems.

Benchtop NMR instruments are low-field, fixed-magnet systems operating at less than 100 MHz. Common commercially available benchtop NMR models will employ magnets that operate at 42, 60, and 82 MHz and deliver sufficient resolution for quality control applications and reaction monitoring.

The convenience of having a benchtop NMR system in the laboratory has been a major influence in the growth of the market, particularly in the pharmaceutical industry. Instead of sending out samples to a core facility and waiting hours for results, pharmaceutical scientists are able to get NMR data almost immediately.

Because the instruments use fixed magnets, unlike with high-field systems, there is no need for cryogenics such as liquid helium or liquid nitrogen. As a result, benchtop NMR instruments have a comparatively low overall cost of ownership.



2016 benchtop NMR demand by sector.

Food laboratories are adopting benchtop NMR systems to determine solid fat content. Other applications include analyzing foods for moisture, carbohydrates, and alcohol content as well as food authenticity or adulteration.

The overall market for low-field and fixed-magnet NMR instruments totaled about \$130 million in 2016. The demand for benchtop NMR systems continues to strengthen, particularly in pharmaceutical quality control applications and the food sector, in which NMR is used to analyze essential oils, fish oils, alcoholic beverages, and fruit juices.

Leading suppliers of benchtop instruments include Bruker, with its minispec TD-NMR instruments, Thermo Fisher Scientific, which entered the market with its acquisition of picoSpin in 2012, Magritek, which recently introduced the Spinsolve 80, and Oxford Instruments, which offers the Pulsar NMR instruments.

Market size and growth estimates were adopted from TDA's *Industry Data*, a database of market profiles from independent market research firm Top-Down Analytics. For more information, contact Glenn Cudiamat, general manager, at (888) 953-5655 or glenn.cudiamat@tdaresearch.com. Glenn is a market research expert who has been covering the analytical instrumentation industry for nearly two decades.



Better Digestions. Better Analyses.

cem.com/mars6

New technologies to meet the demands of your analytical laboratory.



iWave

Light Emitting Technology

True internal temperature control
without probes.



iPrep

Unmatched Vessel Performance

The highest performing vessel ever
developed with dual-seal technology.





Atomic Perspectives

Our Daily Dose of Poison: A Look at Lead in the Food Supply

This month's "Atomic Perspectives" examines current research concerning lead in the United States food supply as well as investigations using inductively coupled plasma–mass spectrometry (ICP-MS) carried out by the author into the measurement of high concentrations of lead in food items, which in many cases far exceeded the levels found in the drinking water supply in Flint, Michigan. The study also briefly covers some history of lead use and the challenges and limitations of setting advisory limits and guidelines.

Patricia Atkins

Lead is one of the most documented and ubiquitous toxic substances in the world present in soil, plants, water, and air. Industrial activities and lead products transitioned a mostly immobile element into a highly dispersed toxic pollutant. In 2016, people in the United States were shocked over the high lead levels detected in the drinking water supply in Flint, Michigan. The analytical testing community was concerned, but not truly surprised. The bigger surprise for scientists was the public reaction to this one incident rather than the thousands of other cases of lead exposure the scientific community uncovers each year. Over the centuries, lead has been dispersed by daily use of lead products, factory emissions, gasoline combustion, paint decay, pesticide application, and other industrial uses.

Historical Perspective

The earliest instances of the use of lead came from Asia Minor where small lead beads were discovered dating back to about 6500 BCE. The early Egyptians used lead to glaze their earthenware and applied lead cosmetics. Recently, studies have suggested they mixed multiple forms of lead such as galena, cerussite, laurionite, and phosgenite in the cosmetic, kohl, to ward off illnesses. The antibacterial

properties of these compounds may have played a role in that belief (1).

Ancient Greeks were experts in the process of converting lead ore to white lead (basic lead carbonate), which became the base pigment for paints, coatings, and cosmetics for centuries. Lead was an appealing metal to work with because of its low melting point and ability to bond easily with other elements. It was resistant to corrosion and inexpensive to obtain because it was a common by-product of gold and silver mining.

The Romans expanded lead use to between 60,000 to 80,000 tons of lead per year at peak production. Romans used lead in all of their daily activities in applications ranging from water pipes to tableware and cosmetics. Lead "sugar" (lead [II] acetate) was a popular additive to food and drinks to sweeten possibly sour or spoiled food. Another popular sweetener, sapa, was grape juice syrup reduced in lead pots to produce the sweet taste not found by using copper or brass cookware. It is suggested that the average Roman's daily exposure from all sources of lead was between 35 and 250 mg/day (2).

Despite the widespread use of lead, there were indications that ancient physicians and scholars were aware of its potential toxicity. In 400 BCE, Hippocrates described

Table 1: Comparison of established regulatory limits for lead in water and results from Flint, Michigan, water samples

Source	FDA	EPA	EU/WHO	Cited Ref.	Detroit Lake Huron	Flint	Flint	Flint	EPA
Form	Bottled water	Drinking water action level	Drinking water action level	Concentration of concern for lead exposure	90th percentile results	90th percentile results	High result (VT sample)	Highest recorded sample	Designation for toxic waste concentration
Pb ($\mu\text{g/L}$)	5	15	10	5	2.3	27	158	13000	5000

symptoms and illnesses related to the consumption of lead-laden food and wine. In 250 BCE, the Greek poet and physician, Nikander of Colophon, reported cases of anemia, colic, and paralysis from lead poisoning. Throughout the Roman Empire, gout, thought to be caused by lead, plagued the affluent classes. In the ancient world, lead poisoning was a disease of either the wealthy who could afford luxuries such as lead-lined wine casks, pewter dinnerware, and lead-laden cosmetics or the slaves exposed to lead in the mines and refineries.

Industrial Uses

Lead use continued through the subsequent centuries, albeit at a decreased amount after the fall of the Roman Empire. The middle ages saw the use of lead to create glass, bullets, and cosmetics to create the pale, white appearance popularized by Queen Elizabeth I. As new worlds were discovered, the mining of lead expanded to North America with the first mine established in 1621 in Virginia. Lead production increased dramatically with the dawn of the Industrial Revolution. Great Britain's production surpassed the levels seen at the height of the Roman Empire's production. By 1900, the United States had surpassed the United Kingdom in lead production to meet the world's increasing demand, which had grown dramatically from Rome's peak production of 80,000 tons per year to over 11 million tons per year by 2016 (3).

Many of the modern sources of lead pollution are our inheritance and will be our legacy. During the industrial revolution through the beginning of the 20th century, the largest sources of lead were industrial emissions and lead products. This exposure distribution dramatically changed during the 1920s

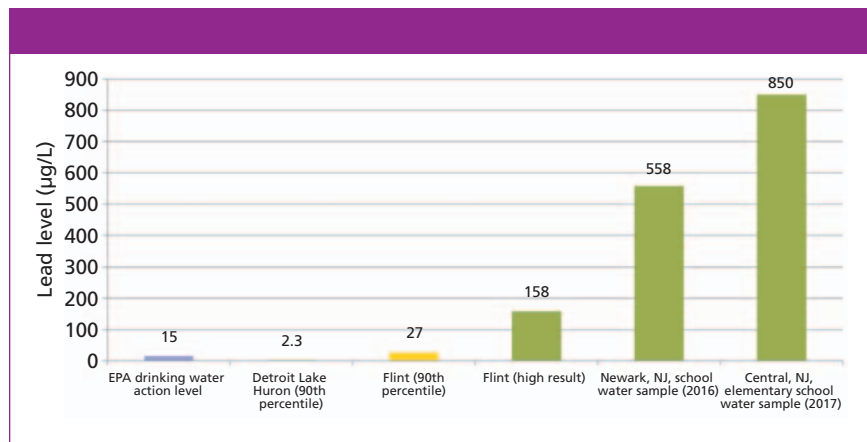


Figure 1: Comparison of lead levels found in Flint water samples and New Jersey school water sources in 2015–2017 ($\mu\text{g/L}$).

with the introduction of tetraethyl lead (TEL) into automotive gasoline. From that point onward, the largest sources of lead exposure became automotive emissions and lead paint. The addition of TEL to gasoline has been described as one of the greatest public health failures of the 20th century.

Leaded Gasoline and Paint

In the 1850s, TEL was discovered by a chemistry professor at the University of Zurich named Carl Jacob Löwig. During the 1920s, automakers saw stiff competition in the race to increase engine performance. A General Motors chemist, Thomas A. Midgley, found that the addition of TEL allowed engines to run without knocking, and a new product called ethyl gas was born. From the outset, many concerns were voiced by scientists familiar with the product. Letters were written objecting to the use of the toxic element. By the 1920s, the dangers of lead were well known. The first U.S. childhood death attributed to lead paint had been reported in 1914 and by the time of the launch of ethyl gas, the League of Nations had banned lead interior paint. By the mid-1930s and 1940s the use of

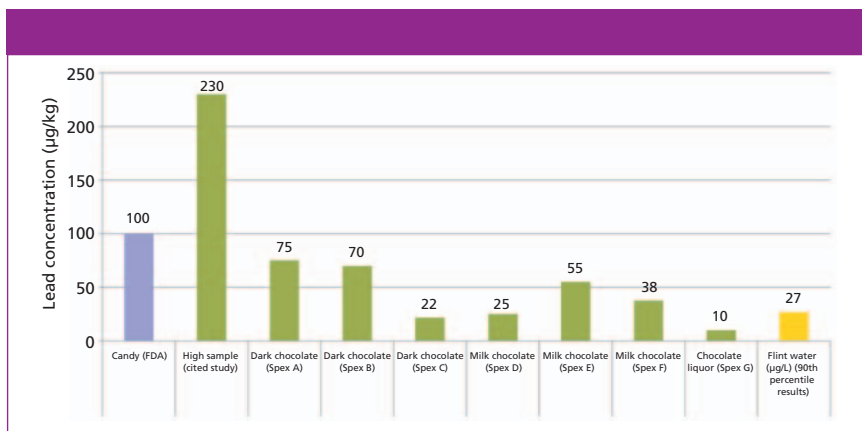
leaded gasoline was firmly entrenched in the automotive industry.

Just a century after its discovery, TEL became a major pollutant in the world. Despite growing health questions, in 1959, the U.S. Public Health Service approved a request to increase lead levels in Ethyl Corp.'s gasoline. The 1960s saw the first investigations and hearings into the restriction of lead in gasoline, but it wasn't until 1980 that an official phase-out was enacted. In 1980, the National Academy of Sciences stated that leaded gasoline was the greatest source of lead pollution in the atmosphere and it was estimated that the daily intake was approximately 0.3 mg per person from this pollution.

Unfortunately, our inherited legacy of lead persists. Many buildings have decades if not centuries of lead paint or were constructed with lead plumbing. One of the primary routes of lead poisoning today in children is exposure through household and neighborhood dust and dirt that contains leaded automotive residues and deteriorating lead paint (4). Urban cities with high populations and dense traffic bear the highest lead burden. Studies in New Orleans, Louisiana,

Table II: Regulatory limits for lead in select ingestible products

Source	FDA	EPA	FDA	FDA	AHPA (2012)	ATSDR	USP <232>	USP <2232>
Form	Bottled water	Drinking water action level	Candy	Juice	Oral supplements	Oral dosage	Oral mediations	Dietary supplements
Units	µg/L	µg/L	µg/kg	µg/L	Daily oral dosage limit (µg)	Daily µg calculated to body weight (70-kg adult)	Daily oral dosage limit (µg)	Daily oral dosage limit (µg)
Pb	5	15	100	50	6	10	5	5

**Figure 2: Lead concentration (µg/kg) found in chocolate samples and FDA limit for candy.**

and Saint Paul, Minnesota, showed that the cities with higher automotive congestion could have anywhere between 100 to 1200 µg/g of lead in the soil, whereas the suburban areas were found to have less than 75 µg/g of lead in the soil on average (5).

Drinking Water

Another major route of lead ingestion for children is drinking water. Lead enters the drinking water in a variety of means, but one prevalent method is lead from plumbing. Water leaches the lead from old pipes and contaminates the water. A second route of lead entering the drinking water is the contamination of the ground water by residual lead sources (dust, dirt, paint, old pesticides, and so on). The 1974 Clean Water Act transferred governance over drinking water to the federal government. The United States Environmental Protection Agency (US EPA), acting for the federal government, has imposed restrictions for water quality. In 1991, the Lead and Copper Rule was imposed by the EPA to limit the concentration of lead and copper in public drinking water at the consumer's tap.

The rule also issues guidelines regarding the amount of lead and copper that can be released through pipe corrosion. The action level for lead is 15 µg/L. If a public water supply exceeds the action limit, appropriate treatments must be used to reduce the lead levels to below the action limit.

In 2015 and 2016, the news was filled with the public health disaster that was being uncovered in Flint, Michigan (6). For decades, the city of Flint had obtained their water from the Detroit Water and Sewerage Department (DWSD), which pumped its water from Lake Huron. The DWSD, following the guidelines of the Lead and Copper Rule, treated the water with orthophosphates (often in the form of food-grade phosphoric acid), which coat the water pipes and reduce leaching of lead and copper into the water supply. While Flint was connected to this treated water supply, the lead and copper levels in their drinking water complied with the EPA rules.

Crisis in Flint, Michigan

In 2014, Flint's administration decided to switch the water supply from

Lake Huron to the Flint River. To the local residents, the Flint River was not known as a trustworthy body of water. It had a reputation of being polluted. The water was much more corrosive than the water of Lake Huron. In addition to a lack of organophosphate treatments, the water of the Flint River was treated with ferric chloride to reduce the formation of trihalomethanes from organic matter, which dramatically increased the chloride content and made the water increasingly corrosive.

By April 2014, the city had switched its water supply to the Flint River and soon after, reports of dirty and smelly water started coming into city offices. By the summer of 2015, scientists were finding drinking water with high lead content. In the summer of 2016, scientists at Virginia Tech (VT) began studying lead levels in the Flint water and by the fall had found more than 40% of homes in Flint had high lead levels. In September, they recommended that the state of Michigan should declare the drinking water in Flint unsafe for consumption. The most significant measure of the contamination was the 90th percentile level of lead exposure in homes tested, meaning that 90% of homes would have a lead level below that threshold and 10% would have levels above it. The action level for drinking water is 15 µg/L, and in the Detroit water supply, which was previously connected to Flint, it was measured at 2.3 µg/L. At the time of the crisis, the 90th percentile of Flint's water supply was 27 µg/L with some samples reading over 100 µg/L. One extremely high sample was found to have 13,000 µg/L, which could be defined as toxic waste by the EPA, whose definition is 5000 µg/L (5 ppm) or higher (7) (see Table I).

The public response to the crisis in Flint was one of shock and horror. Demands were made to improve clean water access and the government funds for water quality. The reaction of the scientific community was one of resignation and disappointment. Scientists had been speaking out about lead toxicity for more than a century, but often the reports of lead contamination or poisoning fell on deaf political ears while being quietly logged in the scientific journals. During the past two decades, more than one million articles concerning lead exposure have been published, which equates to almost 150 articles published every day for the past 20 years.

Flint was not the first major lead contamination event in the United States, it was just one of the most publicized. At the height of the Flint controversy, it was revealed by CNBC that the EPA found only nine U.S. states routinely reported safe lead levels in their water supply (8). A total of 41 states had action levels that exceeded the safe lead limit within the last three years. Reuters issued a report at the end of 2016 that more than 3000 areas in the United States had higher lead levels than Flint and some levels were twice as high (9). Toward the end of the news coverage of the crisis in Flint, it was announced that there was a water crisis in schools in Newark, New Jersey, where levels of lead coming from school water sources often exceeded the levels of lead found in Flint (10). Then, in the spring of 2017, parents in an Ocean County, New Jersey, grade school were sent an email message discussing some failure of school water sources because of lead. Buried within the pages of scientific documentation was a grade school water source that was reported to have 30 times more lead than the Flint water (850 ppb) (see Figure 1).

Public Awareness

Most scientists and experts agree that the most positive thing to come from the crisis in Flint is a renewed public awareness focused on lead exposure and the contamination from lead products and legacy infrastructures. Over the past decade, regulatory agen-

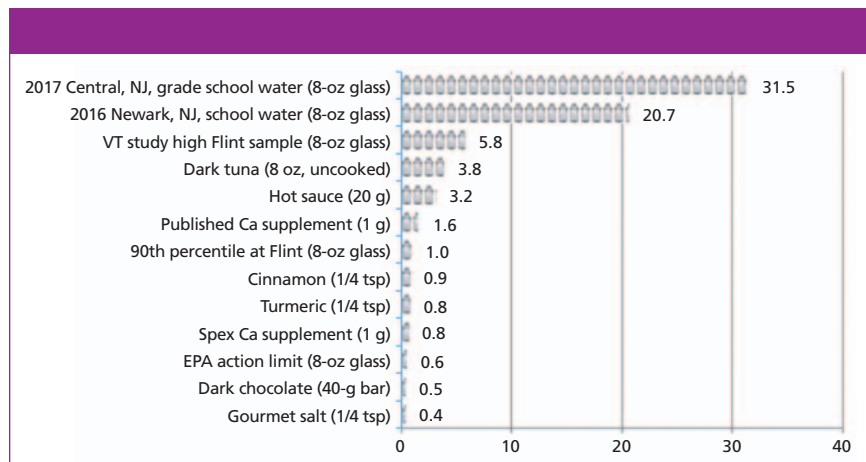


Figure 3: The equivalent volume of Flint water (8-oz glasses) needed to equal the Pb (µg) in a daily dose of ingestible products.

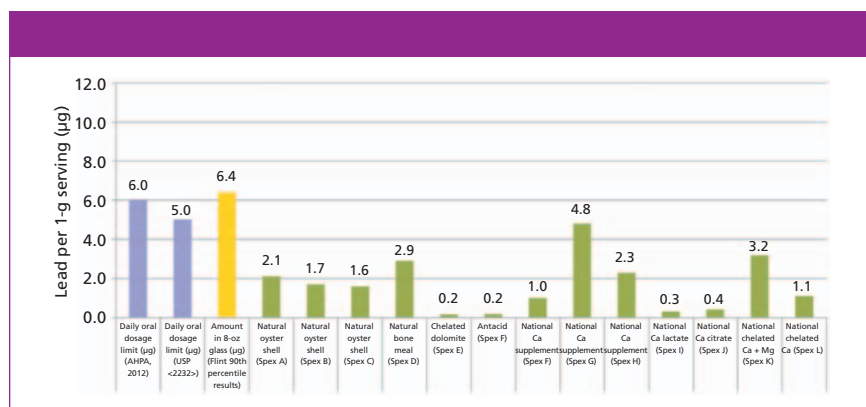


Figure 4: Lead concentration in calcium supplements (µg) in a daily 1-g serving.

cies have started to either issue or re-examine lead limits for common exposure threats (air, water, soil, and dust) and daily ingestible products (food, medications, supplements, water, and food) (see Table II).

Food has not been considered to be the main source of lead intake since the mid-1990s because of the banning of lead solder in canned food and lead seals. But, that does not negate the fact that despite the precautions to limit lead, high amounts are still found in common foods and nutraceuticals. Some of this lead contamination is natural, through bioaccumulation of lead from contaminated soil and water. Lead can accumulate in dense tissues like bones, organs, roots, or seeds and become condensed into dehydrated or processed products (such as nuts, spices, dried fruit, and bone meal).

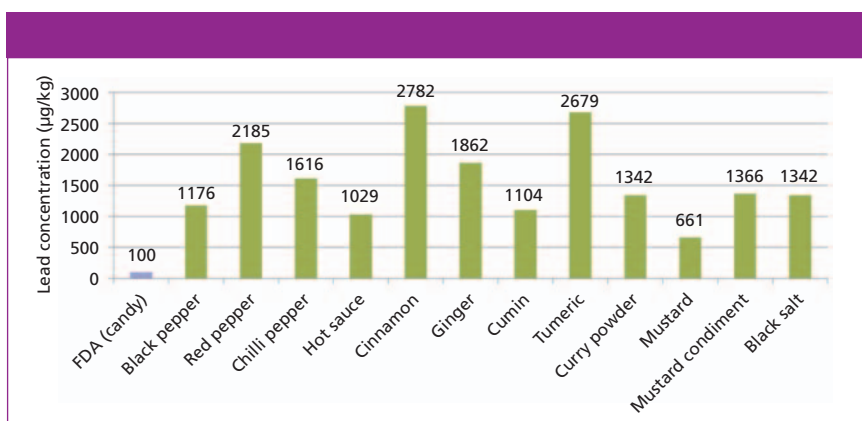
Foodstuffs

A popular food reported to contain

lead is chocolate. Cacao is often grown in regions with historical heavy metal pesticide application. Metals can accumulate in the seed pod used to create chocolate, thereby potentially increasing heavy metal contamination. In 2005, Rankin and colleagues reported lead levels ranging from 0.5 µg/kg to 230 µg/kg in chocolate and cacao samples (11). Spex CertiPrep examined several different types and forms of chocolate and found levels from 10 µg/kg in chocolate liquor to 75 µg/kg in a dark chocolate using inductively coupled plasma–mass spectrometry (ICP-MS) (13). The overall lead concentrations in the chocolate products were all higher than the concentration of lead found in the majority of Flint water samples (Figure 2). The difference is seen in the dosage where the Spex CertiPrep chocolate sample would provide 3 µg of lead in a typical 40 g chocolate bar whereas an 8-oz glass

Table III: Potential lead burden (μg) of daily dose of common ingestible products

Source	Cited Concentration (ppb)	Units	Daily Dose	Pb Daily Dose (μg)
Gourmet salt (1/4 tsp)	1342	$\mu\text{g}/\text{kg}$	1/4 tsp	2.7
Dark chocolate (40 g bar)	75	$\mu\text{g}/\text{kg}$	40 g bar	3.0
EPA action limit (8 oz glass)	15	$\mu\text{g}/\text{L}$	8 oz glass	3.6
Ca supplement (Spex)	4800	$\mu\text{g}/\text{kg}$	1 g tablet	4.8
Turmeric (1/4 tsp)	2700	$\mu\text{g}/\text{kg}$	1/4 tsp	5.4
Cinnamon (1/4 tsp)	2800	$\mu\text{g}/\text{kg}$	1/4 tsp	5.6
90th percentile at Flint (8 oz glass)	27	$\mu\text{g}/\text{L}$	8 oz glass	6.4
Ca supplement (published)	10,000	$\mu\text{g}/\text{kg}$	1 g tablet	10.0
Hot sauce (20 g)	1020	$\mu\text{g}/\text{kg}$	2 - packets (20 g)	20.4
Dark tuna (8 oz uncooked)	110	$\mu\text{g}/\text{kg}$	8 oz raw portion	24.9
High Flint sample (VT study)	158	$\mu\text{g}/\text{L}$	8 oz glass	37.3
Newark, NJ school water (2016)	558	$\mu\text{g}/\text{L}$	8 oz glass	132.0
Central, NJ grade school water (2017)	850	$\mu\text{g}/\text{L}$	8 oz glass	201.1
EPA designation of toxic waste	5000	$\mu\text{g}/\text{kg}$	NA	NA

**Figure 5:** The concentration of lead found in common spices ($\mu\text{g}/\text{kg}$).

of Flint water would provide about 6 μg of lead. Two chocolate bars would equate to the same amount of lead that was found in a glass of Flint water (Figure 3).

Fresh Seafood

A second popular food product exposed to metals contamination is fish. A study of different types of commercially purchased fish showed that although mercury usually is the metal of primary concern in seafood, lead can also be a significant contaminant. Our fish samples, which included tuna, salmon, and swordfish, contained between 7 and 170 $\mu\text{g}/\text{kg}$ of lead. The highest lead was found in the dark tuna (170 $\mu\text{g}/\text{kg}$), which was six times higher than the concentration in the cited 27- $\mu\text{g}/\text{kg}$, 90th percentile Flint sample. This level of lead in seafood would expose a normal adult to almost 40 μg of lead in an

8-oz uncooked portion. This amount would be the equivalent of drinking 1.5 L of the 27-ppb Flint water sample (see Figure 3).

Calcium Supplements

Lead can have an affinity for calcium binding sites, meaning that calcium tissues and products made from them (dairy, bone meal, and calcium supplements) can accumulate high levels of lead. A survey of studies on calcium supplements in 2000 by Scelfo and Flegal in *Environmental Health Perspectives* described a range of lead levels in calcium supplements up to almost 10,000 $\mu\text{g}/\text{kg}$ of supplement (12). At Spex CertiPrep, we conducted a small study on elements in commercial calcium supplements and found lead levels ranging from 170 $\mu\text{g}/\text{kg}$ to a high of 4800 $\mu\text{g}/\text{kg}$ (13). Therefore a 1 g dose of a calcium supplement would add about 5 μg to an adult's

daily exposure of lead, which would be the equivalent to drinking about 6 oz of the Flint water (Figure 4).

Adulteration of Food Materials

An important route of exposure to lead from food comes from intentional adulteration or accidental contamination of food products. Incidents have occurred over the last few years where imported candy from Mexico was found to contain high lead levels. The lead was attributed to several sources ranging from cooking pots and printing ink to the inclusion of spices that were either contaminated or adulterated with lead. The adulteration of food is a growing problem. Billions of dollars are spent each year on adulterated food products such as chocolate, honey, spices, and supplements. Usually, the adulteration does not cause any significant illness but there have been cases where the products have caused illnesses and deaths. In 1994, dozens of people fell ill and several died from Hungarian paprika adulterated with lead oxide.

Common Spices

Spices are one of the most expensive world commodities, which creates motivation for adulteration. Spices can be adulterated or counterfeited in a variety of means from bulking agents and dyes to substitution by look-alike counterfeits. Spex CertiPrep conducted a study on the contamination and adulteration of common spices where

we found that many spices including black pepper, cinnamon, turmeric, and chili peppers contained very high levels of lead and other heavy metals (13). The average amount of lead across all the tested spices was about 1600 µg/kg. The highest levels of lead were found in the cinnamon (2800 µg/kg), turmeric (2700 µg/kg), and red pepper samples (2200 µg/kg) (see Figure 5).

Despite the high concentrations of lead in the spices, in general, the average person consumes a small amount of any one spice; therefore, daily exposure is fairly low. A quarter teaspoon of cinnamon (1.5–2 g) would result in 4–5 µg of lead in a day equivalent to drinking almost a glass of the average Flint water. However, more alarming was the daily exposure to lead from some spice products such as hot sauce. Hot sauce packets were obtained from a Chinese food restaurant. The concentration of lead found in these packets was 1000 µg/kg (see Figure 5). But, the typical amount of hot sauce used was between one and two packets. Each packet contained 10 g of hot sauce, making the actual lead dosage from two packets to be 20 µg, which was the equivalent of drinking 0.75 L of the average Flint water.

The problem of our exposure to lead is a lack of a consensus for tolerable overall intake levels for lead from all sources on a daily, weekly, or monthly basis. Many regulating bodies, while issuing individual limits for circumstances, incidents of exposure, or products, stop short of proposing overall total exposure limits. In the absence of definitive guidelines, it becomes more important to understand lead exposure from the situations or products that are chosen in daily life. If knowing that Chinese hot sauce is going to add 20 µg of lead to your diet (refer to Table III), or that a piece of fish for dinner has almost the same amount of lead as four glasses of the Flint water (see Figure 3), perhaps a different choice might be made.

Final Thoughts

The story of lead in our daily lives has not been properly addressed with the latest public health crisis

in Flint. The real story of lead is our daily exposure and burden from all the sources of lead we come into contact with each day. It is the story of all the states with high lead levels in drinking water. It is the story of all the schools in the United States with outdated lead plumbing, exposing school children to lead in the classroom. Although the high amounts of lead publicized recently puts a face on the problem, it does not adequately show that while a tragic public health event occurred, it did not occur in a vacuum. The crisis also did not show that there are many sources of lead we are exposed to each day. The average person is exposed to more lead than what is in our water. Lead is found in the air and dust we inhale and the food we ingest, in addition to the water we drink. The amount of lead exposure from our drinking water should also be combined with all the other sources to have a better understanding of the total exposure of lead in our daily lives.

References

- (1) I. Tapsoba, S. Arbault, P. Walter, and C. Amatore, *Anal. Chem.* **82**(2), 457–460 (2010). <https://doi.org/10.1021/ac902348g>.
- (2) National Research Council (U.S. Ed.). *Lead in the Human Environment: A Report* (Washington, D.C., National Academy of Sciences, 1980).
- (3) mcs-2017-lead.pdf. (n.d.). Retrieved from <https://minerals.usgs.gov/minerals/pubs/commodity/lead/mcs-2017-lead.pdf>.
- (4) H.W. Mielke, *Lead Perspective* **30**(3), 231–242 (2008).
- (5) K. Schwartz, "The Spatial Distribution of Lead in Urban Residential Soil and Correlations with Urban Land Cover of Baltimore, Maryland," thesis, Rutgers University, New Brunswick, N.J. (2010).
- (6) C. Ingraham, "This is How Toxic Flint's Water Really Is," *Washington Post* (January 15, 2016). Retrieved from <https://www.washingtonpost.com/news/wonk/wp/2016/01/15/this-is-how-toxic-flints-water-really-is/>.
- (7) D.C. Bellinger, *N. Engl. J. Med.*, **374**(12), 1101–1103 (2016). <https://doi.org/10.1056/NEJMp1601013>.

- (8) D. Gusovsky, "America's Water Crisis Goes Beyond Flint, Michigan," *CNBC* (March 24, 2016). Retrieved August 29, 2017, from <https://www.cnb.com/2016/03/24/americas-water-crisis-goes-beyond-flint-michigan.html>.
- (9) M.B. Pell and J. Schneyer, "The Thousands of U.S. Locales Where Lead Poisoning Is Worse Than in Flint," *Off the Charts* (December 19, 2016). Retrieved August 29, 2017, from <http://web.archive.org/web/20170502091728/https://www.reuters.com/investigates/special-report/usa-lead-testing/>.
- (10) S. Ganim and L. Tran, "How Flint, Michigan's Tap Water Became Toxic," *CNN* (January 13, 2016). Retrieved August 29, 2017, from <http://www.cnn.com/2016/01/11/health/toxic-tap-water-flint-michigan/index.html>.
- (11) C.W. Rankin, J.O. Nriagu, J.K. Aggarwal, T.A. Arowolo, K. Adebayo, and A.R. Flegal, *Environ. Health Perspect.* **113**(10), 1344–1348 (2005). <https://doi.org/10.1289/ehp.8009>.
- (12) A.R. Flegal and G.M. Scelfo, *Environ. Health Perspect.* **108**, 309–319 (2000).
- (13) <https://www.spexcertiprep.com/knowledge-base/appnotes-whitepapers>.



Patricia Atkins is a graduate of Douglass College and Rutgers University in New Jersey. She started in the chemical industry with a position as a QC Chemist and lab supervisor for Ciba Specialty chemicals. Patricia later accepted a position conducting research and managing an air pollution research group within Rutgers University's Civil & Environmental Engineering Department. In 2008, Patricia joined SPEX CertiPrep as an application scientist for the certified reference material's division. She spends her time researching industry trends and developing new reference materials.

For more information on this topic, please visit our homepage at: www.spectroscopyonline.com



Chemometrics in Spectroscopy

Calibration Transfer Chemometrics, Part I: Review of the Subject

Calibration transfer involves multiple strategies and mathematical techniques for applying a single calibration database consisting of samples, reference data, and calibration equations to two or more instruments. The instruments used for initial calibration development and transfer may be of like or meaningfully different optical designs. In a two-part series of articles, we take a broad overview of the chemometric and tactical strategies used for the calibration transfer process. Here in part I, the emphasis is on methods that modify the spectra or regression vectors to correct differences between instruments involved in the calibration transfer process. Part II will review calibration transfer mathematics and approaches.

Jerome Workman, Jr., and Howard Mark

Calibration transfer in its purest form allows a calibration to be moved from one instrument to another with statistically retained accuracy and precision (1,2). Ideally, a model developed on one instrument would provide a statistically identical analysis when used on other instruments, without bias or slope adjustments, without additional product samples for standardization, and without product recalibration.

A variety of textbooks and papers exist describing the general methods and history of calibration transfer. Among these are references describing the details of the background, chemometrics, types of instruments, and differences in sample chemistry (3,4). One comprehensive review of calibration transfer presents an overview of the different mathematical methods used for calibration transfer as well as a critical assessment of their validity and applicability (5). The focus of this review was on a description of methods used for transfer of calibrations

for near-infrared (NIR) spectra (5).

We note there are at least four basic strategies that can be used before the calibration modeling step for calibration transfer:

- instrument matching or making instruments truly alike,
- global modeling or developing models that include varying instrumental parameters, sample preparation, and environmental factors in the data before computing the calibration method,
- model updating, which adds samples from each transfer instrument before computing a revised calibration, and
- sensor selection or finding regression variables that are somewhat insensitive to variation in measurement conditions, yet remain sensitive to the analyte signal.

Most of the methods discussed in this column refer to making one set of spectral responses from one instrument similar to a second set of responses from a second

instrument for transfer; these methods would generally be categorized as instrument matching or standardization methods.

Another prominent review of calibration transfer methods describes multiple chemometric techniques used (6). In this review paper, calibration transfer methods are classified as being represented by three main technical approaches:

- by developing more robust calibrations, derived by combining data from multiple instruments and by using spectral pretreatments of that data,
- by modifying calibrations using bias and slope adjustments (the traditional method), and
- by adjusting spectra, using such methods as piecewise direct standardization (PDS) combined with a patented method that requires spectra from transfer sample sets measured on each instrument involved in the transfer experiment (7).

Again, most of the methods described within this column refer to adjusting spectra or coefficients to match instruments.

A comprehensive book chapter presents a review of calibration transfer methods and a critical assessment of the more common methods in terms of applicability and capabilities (8). This chapter focuses on methods for calibration transfer using NIR spectra. It is noted that the methodology described is widely applicable to other analytical measurement techniques (8). Comprehensive reviews of chemometric methods, including calibration transfer, have been published since 1980 as part of the *Fundamental Reviews in Analytical Chemistry* (9). One of the most cited of those fundamental chemometrics reviews delves into multiple topics related to calibration methods and calibration transfer techniques (10).

Comparison of Transfer Methods

A popular and patented technique for transferring calibration models from a reference analytical instrument to a target analytical instrument is demonstrated as a U.S. patent (11). For this technique, a set of diverse transfer samples are measured on a reference

instrument, producing a reference instrument response for each sample. These measurements are repeated for the target instrument, to produce a target instrument response for each transfer sample. One then generates transfer coefficients capable of performing a multivariate estimation of the reference instrument responses for the transfer samples from the target instrument responses for those samples. The transfer coefficients may then be used to convert a target

instrument response for an unknown sample into the equivalent response for the reference instrument. The patent describes piecewise, classical, and inverse transfer techniques. The target instrument responses for the transfer samples are combined with reference instrument responses for the full set of calibration samples, to derive a multivariate prediction model for the target instrument (11).

A research paper describes the transfer of calibration models between



SUPERCHARGE

Your Spectrometer with PIKE Accessories

NEW Catalog Available!

Download today at www.piketech.com

Featured Product

Achieve Full Circle Results

The External Integrating Sphere, new from PIKE Technologies, is the preferred accessory when high-precision reflectivity measurements are required. It is ideal for studying reflection properties of solids, analyzing light scattering of highly absorbing samples and collecting spectra difficult to obtain with standard sampling techniques. Using the spectrometer's external beam, the sphere is positioned outside the sample compartment to accommodate sample sizes from extra-large to small.






Reflection spectrum of water.

To highlight the External Integrating Sphere's sensitivity for low reflectivity measurements, a water spectrum is presented above. Across the spectrum, the reflectivity values are from 1 to less than 6%, and are within 1 percentage point of the theoretical reflectance of water.

Visit our website to learn more about the External Integrating Sphere and our other sphere models.



(608) 274-2721
www.piketech.com
info@piketech.com

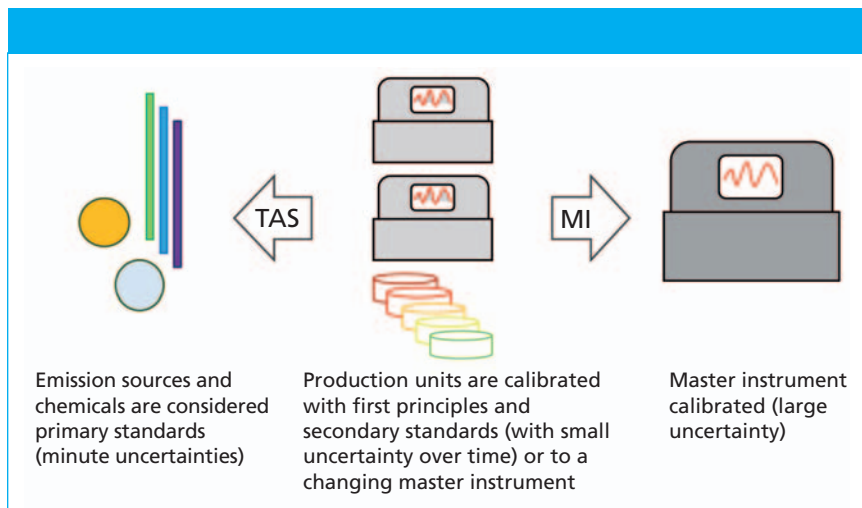


Figure 1: The use of a first physical principles alignment technique provides constant and accurate alignment of all instruments to unchanging physics at any time. The use of a master instrument provides uncertain similarity alignment to the master instrument response that will vary over time.

NIR spectrometric instruments using three different standardization sets representing different sample chemistry types to be used as transfer standards. The first set contained samples that are very similar to the agricultural samples from three different sets to be analyzed, the second set contained generic biological and chemical standards, and the third transfer sample set contained pure organic and inorganic chemicals (12). Another research paper describes several standardization strategies for calibration transfer methods as well as an analysis of problems associated with the choice of the standardization samples (13).

Instrument Alignment and Correction

There are a number of research publications that describe strategies and techniques for instrument alignment and correction (14–18). In these approaches, the instrument wavelength or frequency (X) and photometric (Y) axes are carefully maintained as compared to physical standards so that instrument drift and the differences between instrument wavelength and photometric axes scales are minimized. Full spectrum instruments and research associated with basic instrument measurement technology, instrumentation alignment, mathematical calculations, measuring agreement between instruments, and applying

wavelength and photometric standards are described in a series of papers (19–25). The current state of commercial NIR spectrophotometers and their comparative accuracies are presented in this series. The performance of different instrument types, such as monochromator, Fourier transform, and diode-array-based instruments are compared in detail with data comparisons shown in tabular and graphical forms (19–25). An example of the practical issues associated with multivariate calibration transfer (or calibration transfer) for NIR spectroscopic instruments using reflection spectroscopy for flour analysis was discussed in a recent paper (26). A trademarked and patent pending method that aligns instrument parameters to first principles physics has been described, namely True Alignment Spectroscopy (TAS, Unity Scientific) (27). In this technique, all instrument parameters are aligned to the “true” physical values of first principles standards, such as emission lamps and pure solids, gases, or liquid materials. This method does not rely on a single instrument response function as the standard like what is applied using a “master” instrument concept, but rather relies on basic physical science and the measurement of constant physical standards. Figure 1 illustrates the differences between the concept of first principles alignment and master instrument alignment.

The Master Instrument Concept

The utilization of NIR spectroscopy by the forage and feed industry was initially limited by the requirement to individually calibrate each instrument. Calibration transfer became a necessity for practical application and implementation of NIR over time because of the collection of large, comprehensive databases of more than 1000 or more samples. In the initial application of the “master instrument” concept, 60 sealed samples were used for measurements on primary (“master”) and target (“slave”) instruments for the transfer process. Note that master and slave terms are anachronisms, and have been changed to parent and child instruments, or primary and secondary instruments, respectively. In this method, one monochromator is selected to be the master instrument. Calibration equations are developed on it and transferred to one or more slave instruments. In one publication, six transfer instruments were evaluated (28). The standard errors of difference (SED) including bias among the six transfer instruments for crude protein, acid detergent fiber, neutral detergent fiber, lignin, and in vitro dry matter disappearance were less than the comparative SED among laboratories for reference chemical analysis. It was concluded that satisfactory calibration transfer could be accomplished with 10 samples. This was the most successful and practical method for calibration transfer in the mid-1980s.

Filter Instrument Calibration Transfer

There have been many approaches to correcting instruments for calibration transfer. In one instance, filter instruments were used and a method was demonstrated for computing calibrations that are robust against filter differences and bandwidths of filters. Common methods for wavelength selection involve using absorbance maxima for analyte spectra, using correlation plots relating the change in absorbance with respect to a change in concentration, and using computerized wavelength search algorithms relating to specific

wavelengths and their correlation to changes in concentration.

The technique of selecting isonumeric wavelengths allows the development of general wavelength positions and regression coefficients that are robust against small variations in center wavelength positions for filters because of manufacturing variations. This technique also applies to the wavelength variations that exist in full scanning instruments (29). In the isonumeric method, small changes in wavelength center positions do not affect regression coefficients or the predicted results. To illustrate, given the standard regression equations for every multivariate model expressed in algebraic notation as follows:

$$C_1 = b_{11}A_1 + b_{12}A_2 + bias \quad [1]$$

$$C_2 = b_{21}A_1 + b_{22}A_2 + bias \quad [2]$$

where A_j is the measured absorbance at wavelength j , C_1 and C_2 are the concentrations for samples 1 and 2, and b_{ij} represents the regression coefficients for sample i and wavelength j . The bias is the offset value for the regression.

For the regression coefficients to be immune to wavelength shifts, the following conditions must hold for the regression coefficients b_{11} and b_{12} :

$$\frac{db_{11}}{d\lambda} = \frac{db_{12}}{d\lambda} = 0 \quad [3]$$

An equation derived through a proof in the reference paper leaves the final equation as follows:

$$\sum(Y - \hat{Y}_j)^2 = \sum(Y - \bar{Y})^2 + \sum(\bar{Y} - \hat{Y}_j)^2 \quad [4]$$

where Y is the reference laboratory value and \hat{Y}_j is the predicted value for any sample. The end result of a wavelength search under the conditions that the change in wavelength does not change the regression coefficients, allows the derivation of a calibration equation that is robust against small wavelength shifts within and between instruments.

Direct Standardization and Piecewise Direct Standardization

The second and third most used approaches to multivariate calibra-

tion transfer involve the application of direct standardization (DS) and piecewise direct standardization (PDS) (30–33). These approaches are described in detail with application descriptions, examples, and equations within the cited references. The DS and PDS approaches are also often combined with small adjustments in bias or slope of the predicted values to compensate for small differences not accounted for by using standardization algorithms. Note that the frequency with which standardization approaches must be applied to child instruments is dependent on the frequency of the calibration updates required and the drift of the child instruments with respect to the parent (or original calibration instrument).

PDS was applied to a set of gasoline samples measured on two different NIR spectrometers (34). PDS was applied to a set of two-component samples measured on the same ultraviolet–visible (UV–vis) spectrometer with the use of a cuvette cell with a 10-mm pathlength and a fiber-optic probe with a 2-mm pathlength. Piecewise direct standardization proceeds by determining a structured transformation matrix using the spectra of a few samples measured with both devices. This transformation matrix can then be used to transform any spectrum measured on one device to that obtained on another device, thereby making the calibration model transferable between devices (35). More detailed chemometric improvements to the basic technique of PDS for NIR spectrometric instruments are further described for multivariate calibration transfer in a 1996 paper (36).

For the PDS computation, we apply the following equations:

$$A_{pj} = A_{Cj}b_j \quad [5]$$

where A_{pj} is the response of the standardization samples measured on the parent instrument at wavelength j ; A_{Cj} is the response for the standardization samples measured on the child instrument at wavelength j ; and b_j is the transformation or correction vector of

thermoscientific

discover

solve

assure

What did you
do today?

FTIR • NIR • RAMAN

ThermoFisher
SCIENTIFIC

Find out more at
[thermofisher.com/
solve-is50](http://thermofisher.com/solve-is50)

For Research Use Only. Not for use in diagnostic procedures.

© 2017 Thermo Fisher Scientific Inc. All rights reserved. All trademarks are the property of Thermo Fisher Scientific and its subsidiaries unless otherwise specified. **AD52975 0017**

coefficients for the j th wavelength.

The transformation matrix for PDS is computed using equation 6:

$$\hat{T}_{PDS} = \text{diag} \left(b_1^T, b_2^T, \dots, b_j^T, \dots, b_k^T \right) \quad [6]$$

where k is the total number of wavelengths in the measured standardization samples.

Finally, the response prediction equation for any unknown sample measured on the child instrument is estimated using equation 7:

$$\hat{a}^T = \hat{a}^T_{PDS} \quad [7]$$

For the DS method, the test sample set is measured on the parent and child instruments as typically absorbance (A) with respect to wavelength (k). The spectral data have k individual wavelengths. A transformation matrix (T) is used to match the child instrument data (A_C) to the parent instrument data (A_p). And so equation 8 demonstrates the matrix notation. Note that for DS a linear relationship is assumed between the parent and child measurement values.

$$A_p = A_C \hat{T} + E \quad [8]$$

In equation 8, A_p is the parent data for the test sample set as an $n \times k$ matrix (n samples and k wavelengths), A_C is the child instrument data for the test samples as an $n \times k$ matrix, \hat{T} is the $k \times k$ transformation matrix, and E is the unmodeled residual error matrix.

The transformation matrix (\hat{T}) is computed as equation 9:

$$\hat{T} = A_C^+ A_p \quad [9]$$

where A_C^+ is the pseudoinverse approximated using singular value decomposition of the $n \times k$ spectral data matrix for a set of transfer or standardization samples measured on the child instrument, and A_p is the $n \times k$ spectral data matrix for the same set of transfer or standardization samples measured on the parent instrument. The transform matrix is used to convert a single spectrum measured on the child instrument to be converted to “look” like a parent instrument spectrum.

The response vector for a new measured sample designated as a is predicted using the original model equation as follows:

$$\hat{a}^T = a^T \hat{T} \quad [10]$$

where superscript T is the matrix transpose and \hat{a} represents the estimated or predicted value for the measured sample a .

For the PDS method, the DS method is used piecewise or with a spectral windowing method to more closely match the spectral nuances and varying resolution and lineshape of spectra across the full spectral region, and there is no assumption of linearity between the parent and child prediction results. The transformation matrix is formed in an iterative manner across multiple windows of the spectral data in a piecewise fashion. Many other approaches have been published and compared, but for many users these are not practicable or have not been adopted for various reasons; basic method comparisons are demonstrated in the literature (37).

Orthogonal Signal Correction

An example of orthogonal signal correction (OSC) was applied to NIR spectra that were used in a calibration for the water content in a pharmaceutical product (38). Partial least squares (PLS) calibrations were then compared to other calibration models with uncorrected spectra, models with spectra subjected to multiplicative signal correction, and a number of other transfer methods. The performance of OSC was on the same level as for piecewise direct standardization and spectral offset correction for each individual instrument and PLS models with both instruments included.

The goal of OSC is to remove variation from the spectral data, A , that are orthogonal to Y . This orthogonal variation is modeled by additional components for A and results in the decomposition as shown in equation 11:

$$A = t \cdot p' + t_o p_o' + e \quad [11]$$

where t_o and p_o represent the scores and loadings for the orthogonal component and e is the residual. By removing the Y -orthogonal variation from the data via $A - t_o p_o'$, OSC maximizes correlation and covariance between the X and Y scores to achieve both good prediction and interpretation. As for OSC, there are several algorithms that have been reported in the literature (40). These algorithms differ in the approach used to obtain t_o . For new spectral data, A_{new} , a new score vector is calculated and multiplied with the loading vector (p') computed previously. In the final step, the product of the two is subtracted from A_{new} .

Procrustes Analysis

In analytical chemistry, it is necessary to form instrument-dependent calibration models. Problems such as instrument drift, repair, or use of a new instrument create a need for recalibration. Since recalibration can require considerable costs and cause time delays, methods for calibration transfer have been developed. One paper shows that many of these approaches are based on the statistical procedure known as *procrustes analysis (PA)* (41). Transfer by PA methods is known to involve translation (mean-centering), rotation, and stretching of instrument responses (41). The standard PA steps include translation, uniform scaling, rotation, and fine adjustments to superimposing the signals or spectra. An excellent tutorial on the general use of the procrustes technique in chemistry is found in the literature (42).

Finite Impulse Response

In an example paper, four different calibration transfer techniques are compared (43). Three established techniques, finite impulse response (FIR) filtering, generalized least squares weighting (GLSW), and PDS, were evaluated. A fourth technique, baseline subtraction, was reported to be the most effective for calibration transfer. Using as few as 15 transfer samples, the predictive capability of the analytical method was maintained across multiple instruments and major instru-



What did you do today?

Whether you're discovering new materials, solving analytical problems or assuring product quality, your spectrometer needs to deliver the definitive answers you're looking for — fast! Thermo Fisher Scientific goes beyond your expectations with a full line of FTIR, NIR and Raman spectroscopy systems, to help you move from sample to answer . . . faster than ever before.

The Thermo Scientific™ Nicolet™ iS50 FTIR Spectrometer is your all-in-one materials analysis workstation. With simple one-touch operation and fully-integrated diamond ATR, the Nicolet iS50 gives your lab the productivity you need today and the capabilities you need tomorrow.

Discover. Solve. Assure. thermofisher.com/solve-is50

ThermoFisher
SCIENTIFIC

ment maintenance (43). Previously, a standard-free method using the FIR filter was successfully used to transfer the NIR spectra of caustic brines, analgesics, and terpolymer resins. This example paper carries the FIR transfer method one step further, leading to an improved algorithm that makes the transfer more robust and general by avoiding transfer artifacts in the filtered spectra (44).

In a second example paper, FIR filtering was used for a set of spectra to be transferred, using a spectrum on the target instrument to direct the filtering process (45). Often, the target spectrum is the mean of a calibration set. The method is compared against direct transfer and piecewise direct transfer on NIR reflectance spectra in two representative data sets. Results from these studies suggest that FIR transfer compares favorably with piecewise direct transfer in terms of accuracy and precision of the match of transferred spectra to the predictive calibration models developed on the target instrument. Unlike piecewise direct transfer, FIR transfer requires no measurement of standard samples on both the source and target spectrometers. Details and limitations of the FIR transfer method are presented in the literature (45).

Maximum Likelihood Principal Component Analysis

A calibration transfer method, called *maximum likelihood principal component analysis (MLPCA)*, is analogous to conventional principal component analysis (PCA), but incorporates measurement error variance information in the decomposition of multivariate data (46). A very detailed description of the derivation, computations, and results discussion is given in the literature (47).

Using Wavelength Standards for FT-NIR Alignment

A series of papers describe the use of a powdered mixture of Er_2O_3 , Dy_2O_3 , Ho_2O_3 , and talc measured at a constant resolution of 2 cm^{-1} on four combinations of spectrometers and sampling accessories. The wavenum-

ber scale of each mixture spectrum was corrected with lines in the vibration-rotation spectrum of water vapor to an accuracy better than 0.02 cm^{-1} . The claim for this work is that the reported values for the DR standard are improved by an order of magnitude compared to the values reported by the National Institute of Standards and Technology (NIST). These values for the standard are used for testing or calibrating alignment for the wavelength axis of a spectrometer. A discussion of the various methods, and results, is provided in the literature (48–50) and will be further described in greater detail in subsequent columns on the subject of reference standards.

Summary

There are multiple mathematical techniques being applied for transfer of multivariate calibrations. Some of these techniques were described within this column with appropriate references. In the next installment in this series, we will continue to provide a basic top-level review of calibration transfer methods.

References

- (1) J.J. Workman Jr., in *40 Years of Chemometrics—From Bruce Kowalski to the Future* (American Chemical Society, Washington, D.C., 2015), pp. 257–282.
- (2) H. Mark and J. Workman, *Spectroscopy* **28**(2), 24–37 (2013).
- (3) H. Mark and J. Workman, *Chemometrics in Spectroscopy*, 1st Edition (Elsevier/Academic Press, Boston, Massachusetts, 2010).
- (4) J. Workman, in *The Concise Handbook of Analytical Spectroscopy: Physical Foundations, Techniques, Instrumentation and Data Analysis*, J. Workman, Ed. (World Scientific Publishing-Imperial College Press, in 5 Volumes, UV, Vis, NIR, IR, and Raman, New Jersey and Singapore, 2016), volume 3, pp. 185–188, volume 4, pp. 159–162 (2016).
- (5) R.N. Feudale, N.A. Woody, H. Tan, A.J. Myles, S.D. Brown, and J. Ferré, *Chemom. Intell. Lab. Syst.* **64**(2), 181–192 (2002).
- (6) T. Fearn, *J. Near-Infrared Spectrosc.* **9**(4), 229–244 (2001).

- (7) J. Shenk and M. Westerhaus, U.S. Patent 4,866,644 September 12, 1989.
- (8) S.D. Brown, *Chemom. Intell. Lab. Syst.* **64**(2), 181–192 (2002).
- (9) B.R. Kowalski, *Anal. Chem.* **52**(5), 112R–122R (1980).
- (10) B. Lavine and J. Workman, *Anal. Chem.* **80**(12), 4519–4531 (2008).
- (11) B.R. Kowalski, D.J. Veltkamp, and Y.D. Wang, U.S. Patent 5,459,677 October 17, 1995.
- (12) E. Bouveresse, D.L. Massart, and P. Dardenne, *Anal. Chim. Acta* **297**(3), 405–416 (1994).
- (13) O.E. De Noord, *Chemom. Intell. Lab. Syst.* **25**(2), 85–97 (1994).
- (14) J. Workman, B. Kowalski, and P. Mobley, “The Design of an Expert Calibration System for Spectroscopic Based Process Analytical Chemistry,” presented at 40th Annual ISA Analysis Division Symposium, Toronto, Ontario, Canada, April 1995.
- (15) J. Workman, in *Spectrophotometry, Luminescence and Colour, Science and Compliance*, C. Burgess and D. G. Jones, Eds. (Elsevier, Amsterdam, 1995), pp. 369–384.
- (16) D. Tracy, R. Hoults, and A. Ganz, U.S. Patent 5,303,165 April 12, 1994.
- (17) K. Busch and D. Rabbe, U.S. Patent 6,774,368 August 10, 2004.
- (18) J. Workman Jr. and H. Mark, *Spectroscopy* **30**(7), 32–37,48 (2015).
- (19) J. Workman Jr. and J.P. Coates, *Spectroscopy* **8**(9), 36–42 (1993).
- (20) A. Folch-Fortuny, R. Vitale, O. de Noord, and A. Ferrer, *J. Chemom.* **31**(3), e2874 (2017).
- (21) J. Workman Jr. and H. Mark, *Spectroscopy* **28**(5), 12–25 (2013).
- (22) J. Workman Jr. and H. Mark, *Spectroscopy* **28**(6), 28–35 (2013).
- (23) J. Workman Jr. and H. Mark, *Spectroscopy* **28**(10), 24–33 (2013).
- (24) J. Workman Jr. and H. Mark, *Spectroscopy* **29**(6), 18–27 (2014).
- (25) J. Workman Jr. and H. Mark, *Spectroscopy* **29**(11), 14–21 (2014).
- (26) C. Eskildsen, P. Hansen, T. Skov, F. Marini, and L. Nørgaard, *J. Near Infrared Spectrosc.* **24**(2), 151–156 (2016).
- (27) J. Workman Jr., *NIR News* **27**(3), 12–15 (2016).
- (28) J.S. Shenk, M.O. Westerhaus, and W.C. Templeton, *Crop Science* **25**(1), 159–161 (1985).

- (29) H. Mark and J. Workman Jr., *Spectroscopy* **3**(11), 28–36 (1988).
- (30) Y. Wang, D. Veltkamp, B.R. Kowalski, *Anal. Chem.* **63**(23), 2750–2756 (1991).
- (31) Z. Wang, T. Dean, and B.R. Kowalski, *Anal. Chem.* **67**(14), 2379–2385 (1995).
- (32) L. Zhang, G. Small, and M. Arnold, *Anal. Chem.* **75**(21), 5905–5915 (2003).
- (33) B.R. Kowalski, D. Veltkamp, and Y. Wang, U.S. Patent 5,459,677 October 17, 1995.
- (34) Y. Wang and B.R. Kowalski, *Appl. Spectrosc.* **46**(5), 764–771 (1992).
- (35) C.S. Chen, C.W. Brown, and S.C. Lo, *Appl. Spectrosc.* **51**(5), 744–748 (1997).
- (36) E. Bouveresse and D.L. Massart, *Chemom. Intell. Lab. Syst.* **32**(2), 201–213 (1996).
- (37) X. Luo, A. Ikehata, K. Sashida, S. Piao, T. Okura, and Y. Terada, *J. Near Infrared Spectrosc.* **25**(1), 15–25 (2017).
- (38) J. Sjöblom, O. Svensson, M. Josefson, H. Kullberg, and S. Wold, *Chemom. Intell. Lab. Syst.* **44**(1), 229–244 (1998).
- (39) S. Wold, H. Antti, F. Lindgren, and J. Öhman, *Chemom. Intell. Lab. Syst.* **44**(1), 175–185 (1998).
- (40) H. Goicoechea and A. Olivieri, *Chemom. Intell. Lab. Syst.* **56**(2), 73–81 (2001).
- (41) C.E. Anderson and J.H. Kalivas, *Appl. Spectrosc.* **53**(10), 1268–1276 (1999).
- (42) J.M. Andrade, M. Gómez-Carracedo, W. Krzanowski, and M. Kubista, *Chemom. Intell. Lab. Syst.* **72**(2), 123–132 (2004).
- (43) R.P. Cogdill, C.A. Anderson, and J.K. Drennen, *AAPS PharmSciTech.* **6**(2), E284–E297 (2002).
- (44) H. Tan, S.T. Sum, and S.D. Brown, *Appl. Spectrosc.* **56**(8), 1098–1106 (2002).
- (45) T. Blank, S. Sum, S.D. Brown, and S. Monfre, *Anal. Chem.* **68**(17), 2987–2995 (1996).
- (46) D.T. Andrews and P.D. Wentzell, *Anal. Chim. Acta* **350**(3), 341–352 (1997).
- (47) P. Wentzell, D. Andrews, D. Hamilton, K. Faber, and B.R. Kowalski, *J. Chemom.* **11**(4), 339–366 (1997).
- (48) H. Yang, T. Isaksson, R.S. Jackson, and P.R. Griffiths, *J. Near Infrared Spectrosc.* **11**(4), 229–240 (2003).
- (49) H. Yang, T. Isaksson, R.S. Jackson, and P.R. Griffiths, *J. Near Infrared Spectrosc.* **11**(4), 241–255 (2003).
- (50) T. Isaksson, H. Yang, G.J. Kemeny, R.S. Jackson, Q. Wang, M.K. Alam, and P.R. Griffiths, *Appl. Spectrosc.* **57**(2), 176–185 (2003).



Jerome Workman Jr. serves on the Editorial Advisory Board of *Spectroscopy* and is the Executive Vice President of Engineering at Unity Scientific, LLC, in Milford, Massachusetts. He is also an adjunct professor at U.S. National University in La Jolla, California.



Howard Mark serves on the Editorial Advisory Board of *Spectroscopy* and runs a consulting service, Mark Electronics, in Suffern, New York. Direct correspondence to: SpectroscopyEdit@UBM.com

For more information on this topic, please visit:
www.spectroscopyonline.com

New Version!

ORIGIN® 2017

Graphing & Analysis

Over 100 New Features & Apps in Origin 2017!

Over 500,000 registered users worldwide in:

- 6,000+ Companies including 20+ Fortune Global 500
- 6,500+ Colleges & Universities
- 3,000+ Government Agencies & Research Labs

For a **FREE 60-day** evaluation, go to OriginLab.Com/demo and enter code: 2187

25+ years serving the scientific & engineering community



Lasers and Optics Interface

Combining Broadband Spectra and Machine Learning to Derive Material Properties

A quiet but interesting trend has been occurring in material analysis, coincident with the rise of artificial intelligence (AI) and so-called “deep” machine learning methods. Astute spectroscopists have always known that there is more information in the spectra that they obtain than simply the molecular or atomic peaks that are directly measured. Particularly with methods such as infrared, Raman, and laser-induced breakdown spectroscopy (LIBS), the spectral background contains a wealth of information about the sample, and analytical combinations of the peaks can provide material properties. Traditionally, such analytical combinations of peaks were performed explicitly by analysts, but now information about material properties embedded in the spectra can be derived implicitly by AI and machine learning algorithms. This column introduces these ideas and touches on recent results indicative of what more may be coming in this direction.

Steve Buckley

Computer calibration and learning technologies go by a variety of different names, depending as much on the application as on the algorithms used. *Machine learning* in its broadest sense refers to the automation of learning without an explicit program, and is used for everything from image recognition and voice recognition to stock selection. In many cases, the machine-learning algorithm is selected with some knowledge of the mathematical characteristics of the problem to assist in performance. *Deep learning* refers to the subset of machine learning that uses a model learning representation rather than a task-specific

algorithm. An example of deep learning could be a neural network or other biological model. *Chemometrics* usually refers to multivariate statistics and machine-learning algorithms applied to chemical and biological systems to extract information. Finally, *artificial intelligence (AI)* may be described as machine intelligence, the expression of some problem solving or learning ability (typically in a narrow area) that humans would equate with cognition. The best-known recent example of AI may be IBM’s Watson computer, which has beaten chess grandmasters and reigning champions on the popular game show *Jeopardy*.

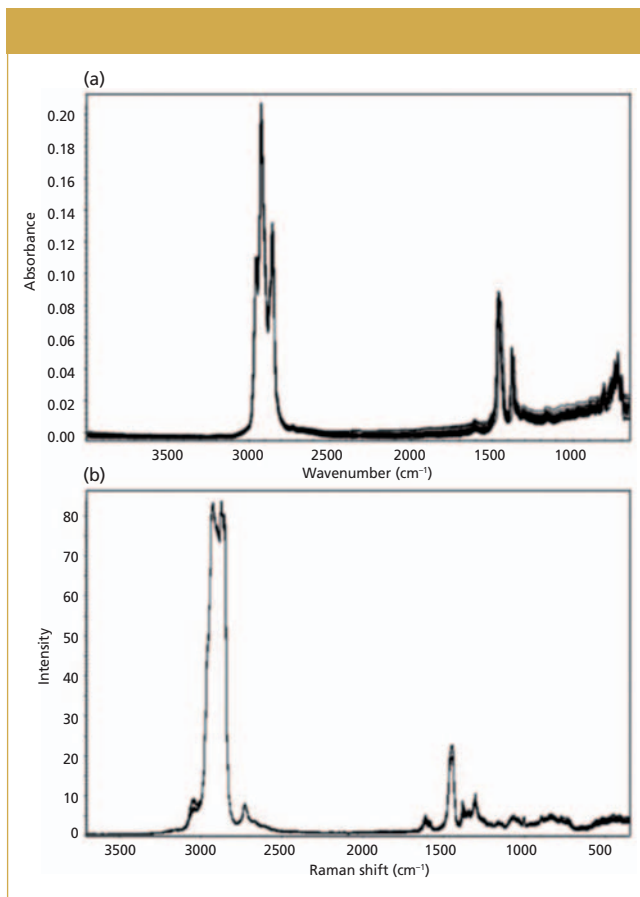


Figure 1: Typical spectra of diesel fuels: (a) FT-IR-ATR, (b) FT-Raman. Adapted with permission from reference 1, under the Budapest Open Access Initiative.

When we make the shift from traditional methods of calibration and analysis to chemometrics, we gain power at the expense of complexity and opaqueness of the model. Previously, to use an atomic spectroscopy example, if we were to build a calibration for chromium in an arc-spark spectroscopy system, we would find a promising emission line that varied predictably over the required range. We would measure the integrated intensity of that background-subtracted Cr emission line over the range, and build a calibration curve that allows prediction of the Cr concentration from the strength of the emission line. Multivariate methods such as partial least squares (PLS) regression or principal components regression build the calibration curve using multiple input variables, which may be positively or negatively correlated with the element being predicted. Extending our chromium example, multiple lines of Cr would be positively correlated with the concentration of Cr in a prediction. In the case of a stainless steel, which may have chromium concentrations of 1–20%, iron concentration may actually vary inversely with Cr concentration. We would then see a negative correlation between Fe emission lines and Cr concentration that could be used in a multivariate model. Using these algorithms we can easily back out specific relationships (negative

Alluxa

REASONS ALLUXA SHOULD BE YOUR OPTICAL COATING PARTNER

- 1 HIGHEST PERFORMANCE**
THIN FILM COATING PROCESS
- 2 ULTRA SERIES BANDPASS, DICHROICS, AND MULTIBANDS**
- 3 HIGH PERFORMANCE**
FLAT-TOP ULTRA NARROWBAND FILTERS
- 4 FASTEST**
CUSTOM COATING TURNAROUND

www.alluxa.com

Table I: Results of diesel property prediction from FT-ATR spectra with an ANN, derived from reference 1

Property	Mean Absolute Error/ Median Measurement (%)	R^2 (Pearson Correlation Coefficient)
Cetane number	0.61%	0.9597
Density	0.09%	0.9315
Viscosity	2.18%	0.9815
Total aromatics	1.99%	0.9662
PAH	7.31%	0.9343

or positive correlations) in the regression model corresponding to each input.

Increasing in complexity and opaqueness, examples of ensemble learning include support vector machine (SVM) and random forest methods for classification and regression. These methods use large quantities of labeled (or quantified) training data to build predictions. In SVM, data are projected into a new coordinate system such that dividing hyperplanes can be used to build categories or regression steps in the data. In random forests, many decision trees are built during classification using subsets of the data, and the classification or regression answer is found by selecting the most frequent (mode) of the prediction. Both of these methods are well-suited to complex, nonlinear problems. However, after a prediction is made, it is nearly impossible to get “inside” the algorithm to determine the relationship between a specific input variable and the prediction, short of a Monte Carlo-type simulation.

Finally, artificial neural networks (ANNs) mimic animal brains, with connections between different neuronal layers doing the processing. One of the first types of AI, pioneered in the 1950s, it has only been in recent years that the power of ANNs could be fully exploited as sufficiently powerful computational resources have been developed. In an ANN, a number of inputs (which could be points in a spectrum) are input. Each input is sent separately to nodes in a “hidden layer.” At the hidden layer, the inputs are combined, using weights for each input that are determined by training.

The outputs of the hidden layer may go directly to the output of the model (prediction), or to a second, and third hidden layer, and so on, before the output. The structure of the network between the hidden layers and the method of determining the weightings can also be variable. Similar to the SVM and random forest, it is difficult if not impossible to unpack the “training” of an ANN into logical steps.

Examples

Recently, researchers have used tools ranging from multivariate methods to ANNs to solve complex spectroscopic problems involving material properties. Here, we explore a few examples that point to how this is accomplished in practice.

Raman and Infrared Spectra Determine Diesel Fuel Properties

Diesel fuel is not uniform, but in the case of petroleum-derived diesel, it typically comprises carbon chains between 8 and 21 carbon atoms in length. Diesel can also be derived from biomass, coal liquefaction, and even animal sources. Given the variety of sources, property measurement is important because no standard formulation exists. In blending diesel fuel, properties such as viscosity, density, and ignition characteristics are key parameters. Viscosity and density determine the flow rate at a given manifold pressure through the injectors, and influence the droplet size and dispersion, related to the spray characteristics. The ignition characteristics are measured through the cetane number (CN), which is a measure of the compression-ignition characteristic of the fuel. The higher the CN, the faster the combustion

and the lower on the temperature–pressure curve the fuel will ignite. Cetane (hexadecane) is easy to ignite and is given the arbitrary number of 100, while typical diesel fuel in the United States has a cetane number between 40 and 55.

The measurement of density is simple, the measurement of viscosity is only slightly harder, but the measurement of CN is actually quite involved. Originally, the fuel in question had to be burned in a special test engine while varying the compression ratio of the engine to achieve a specific ignition delay. From this data, the CN could be calculated. A simpler fuel ignition tester is now used to determine ignition delay and thus the CN, but it still requires a combustion measurement.

Bolanča and coworkers decided to use Fourier transform-infrared-attenuated total reflection (FT-IR-ATR) and FT-Raman spectra of fuels combined with artificial neural networks to try to predict these fuel properties (1). For both methods, spectra included both the fundamental C-H stretch region and the fingerprint region, because the spectra were roughly in the 500–4000 cm^{-1} range. Typical spectra are shown in Figure 1.

These researchers found that, in general, both FT-ATR and FT-Raman methods were able to predict properties with an accuracy approximately equivalent to the uncertainty of the standard test methods, when the 45 samples in the training set were fed into an artificial neural net with a multilayer perceptron model and eight hidden layers. For everything except polycyclic aromatic hydrocarbon (PAH) prediction, the FT-ATR data performed slightly better than the FT-Raman data. Table I shows the results of the best-performing model with the FT-ATR data as shown in Figure 1a.

Determination of Coal Properties Using Laser-Induced Breakdown Spectroscopy

As a naturally occurring, relatively unrefined fuel, coal exhibits a wide

As computing power and memory continue to increase, we should be thinking about how to generate enough of the right kinds of data to feed machine learning algorithms.

range in the properties that are most important for combustion. The primary properties of coal measured in a “proximate” analysis include the heating value (MJ/kg), volatile matter (%), fixed carbon (%), and ash (%), among others. Standard laboratory measurements exist for each of these crucial parameters; typical analysis may take

6 h or more to complete. It would be useful to have a real-time, or nearly real-time, analysis method that could be used for sorting coal by quality at the mine site, blending coal efficiently, spot-checking coal quality for transactions, and control of coal firing in boilers. In particular, more efficient coal firing could help reduce particulate matter and greenhouse gas pollution from coal utilization.

Wang and colleagues at Tsinghua University have published several papers on coal property determination from laser-induced breakdown spectroscopy (LIBS) spectra using a modified “dominant factor” PLS method. The most recent paper (2) describes a spectral normalization method designed to remove the shot-to-shot fluctuation from individual LIBS spectra taken on the same sample, which can be caused by local material changes or laser fluctuations, which affect ablation efficiency and electron

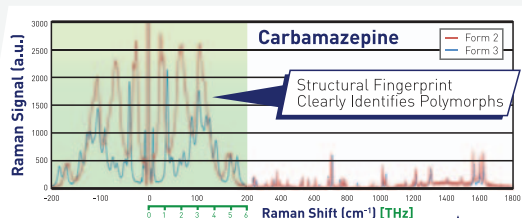
density in the plasma. Following spectral normalization to obtain a “standardized” spectrum, a subset of lines known to be physically related to the desired quantity (called the *dominant factors*) is used in an initial PLS prediction to estimate the property in question. An example of dominant factors might be elemental emission lines associated with minerals for prediction of ash percentage. In training, the dominant factor PLS estimate, which is much more accurate than typical PLS with the entire spectrum, is compared with the known quantity. The entire spectrum is fed into a secondary PLS to determine a “correction” signal, so that the trained algorithm uses both a PLS based on the dominant factors and on the entire LIBS spectrum to arrive at a property prediction. In this case, after a prediction is made the result is stored in a database so that if the same sample is encountered again, it can be recalled, significantly re-

ONDAX

RAMAN SPECTROSCOPY PRODUCTS

See what you've been missing with THz-Raman®

Structural Fingerprint Chemical Fingerprint



Both Stokes and anti-Stokes signals down to 5cm⁻¹

Complete chemical fingerprint

THz-Raman Ultra-low Frequency THz-Raman® Systems & Notch Filters



SureLock

CleanLine

Specializing in low-frequency Raman Systems and Components
Wavelength Stabilized and Single Frequency Lasers from 405nm to 1064nm



ONDAX Online Store

Advanced Solutions for Optical Measurements

850 E. Duarte Rd. Monrovia, CA 91016
T. 626.357.9600 (Tel) | F. 626.513.7494 | sales@ondax.com

© 2017 Ondax, Inc.

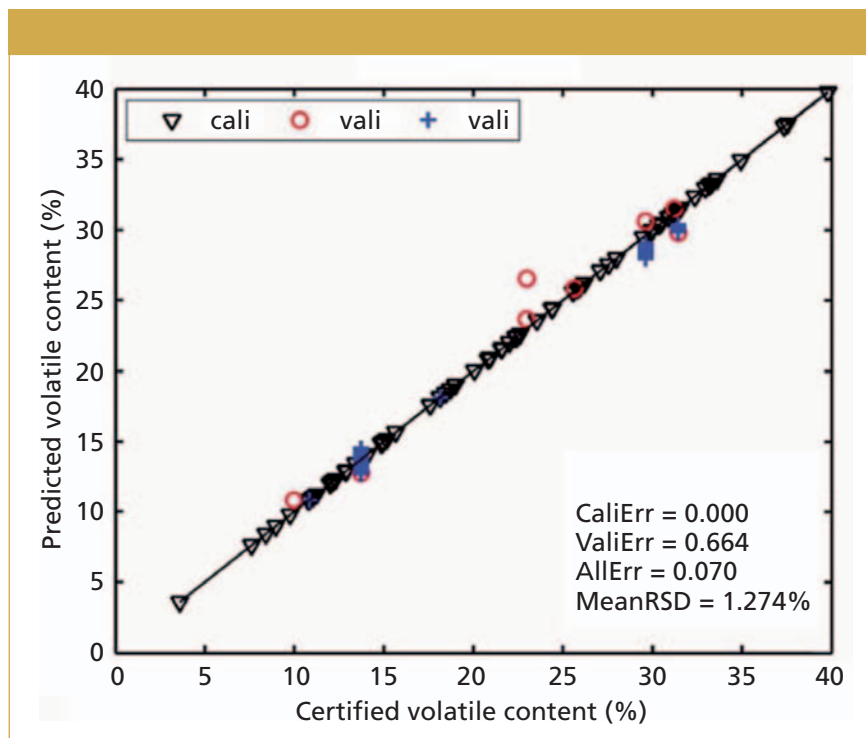


Figure 2: Calibration and prediction of volatile matter in 77 coal samples. Adapted from reference 2 with permission from the Royal Society of Chemistry.

Table II: Summary results on selected coal property measurements with LIBS, from reference 2

Error Associated with	PLS on Entire Spectrum	Dominant Factor PLS Coupled with Database	Chinese National Standard
Carbon measurement	4.9%	0.42%	<1%
Ash measurement (15% < ash < 30%)	1.8%	0.17%	<0.5%
Volatile measurement (20% < volatiles < 40%)	1.69%	0.11%	<0.5%
Heating value measurement	1.1 MJ/kg	0.07 MJ/kg	<0.3 MJ/kg

Table III: Accuracy of classification of jet fuels into "high," "medium," and "low" categories for each of the properties listed, from reference 3

	Flash Point	Freezing Point	Boiling Point (50% v/v)
FuRes (%)	99 ± 1	99 ± 1	98 ± 1
SVM (%)	98.2 ± 0.9	98 ± 2	96 ± 2

ducing shot-to-shot variation on the same sample.

Figure 2 illustrates prediction of volatile matter in coal using the dominant factor PLS model. Like the heating value, volatile matter is one of the coal properties that is more unrelated to the individual elements. Most volatile matter is made up of carbon and hydrogen atoms, but these can also be found in fixed forms in the coal. Hence

the chemometric algorithm needs to do the heavy lifting to find the patterns in the spectrum that correspond to volatile versus fixed forms of hydrocarbons. In Figure 2, the black triangles show the calibration data, and the blue and red symbols show the validation data. For all of the properties mentioned, selected summary results are shown in Table II, compared with PLS on the entire spectrum and compared to the

Chinese National Standard for coal measurements.

Measurement of Jet Fuel Properties in the Near Infrared

Given the requirements for safety, jet fuel is under rigorous specifications for properties such as flash point, freezing point, and boiling point, which are surrogates that indicate the combustion properties of the fuel. These properties may slowly change over time, as well as by batch of fuel received or by contamination. Therefore, rapid measurement of these properties is useful. Xu and colleagues conducted a near-infrared (NIR) study of jet fuels (3) comparing a standard partial least squares-discriminant analysis (PLS-DA) method to a fuzzy rule-building expert system (FuRES) (4) and a support vector machine (SVM). The FuRES is a type of minimal neural network architecture. The SVM and the FuRES had similar performance, significantly better than the PLS-DA method.

The sample set consisted of 49 samples of jet fuel sampled in triplicate. The goal was to classify the previously mentioned temperature properties into "low," "medium," and "high" ranges. Table III illustrates the prediction accuracies for these fuel properties.

Implications

The writing on the wall is clear. As computing power and memory continue to increase, we should be thinking about how to generate enough of the right kinds of data to feed machine learning algorithms. PLS and principal components analysis, which are widely used, only scratch the surface of what is possible. Algorithms that are better able to handle nonlinear, multifactor data such as SVM or random forests may prove useful. Genetic optimization and Bayesian inference also may reveal a lot in the data, and allow us to experiment more efficiently and converge more quickly on an answer. As spectroscopists, we should be learning the pluses and minuses of each of the key methods of machine learning,

We should be asking ourselves which problems would benefit from machine learning, and elevating our game thereby.

or at least making friends with the data scientists, so that we can get the most out of our data. There is a wealth of great references, with one of the most engaging entrees to machine learning being Pedro Domingo's *The Master Algorithm*, which clearly explains the various branches of machine learning, their strengths, and the search for combinations of learning algorithms to enhance AI overall (5).

Data quality is still paramount. No amount of computer processing can yield great results from non-existent or poorly acquired data. However, it is true that properly applied algorithms can sometimes pull a rabbit out of the hat, or the signal from the noise. As we have tried to indicate here, machine learning methods can often pull surprising macro properties out of spectra that we would have suspected of only having elemental and molecular data in the past. The key thing for training such algorithms is good quality data, and often lots of it taken over time.

Several years ago, Google started a focused effort to train image recognition to recognize cats from the millions upon millions of cat (and non-cat) images on its search engine. Now Google's image search can equal or outperform a human in many image recognition tasks. Deep learning algorithms can outperform pathologists in detecting some cancers, and Microsoft Research announced in August that its algorithms can equal or surpass human translators on the classic "Switchboard" conversational speech recognition task, transcrib-

ing real conversations. All of these tasks involve massive amounts of training and computational data at the outset, but once the model is made the task becomes automated and easy.

As spectroscopists, we are good at getting quality data. We should be asking ourselves which problems would benefit from machine learning, and elevating our game thereby. As these examples show, it is likely that we can push the boundaries—measuring new properties and detecting new things—by harnessing the power of AI.

References

- (1) T. Bolanca, S. Marinovic, Š. Ukic, A. Jukic, and V. Rukavina, *Acta Chim. Slov.* **59**, 249–257 (2012).
- (2) Z. Hou, Z. Wang, T. Yuan, J. Liu, Z. Li, and W. Ni, *J. Anal. At. Spectrom.* **31**(3), 722–736 (2016).
- (3) Z. Xu, C.E. Bunker, and P.d.B. Harrington, *Appl. Spectrosc.* **64**(11), 1251–1258 (2010).

- (4) P.d.B. Harrington, *J. Chemom.* **5**(5), 467–486 (1991).
- (5) P. Domingos, *The Master Algorithm* (Basic Books, New York, 2015), pp. 329.



Steve Buckley, PhD,

is the CEO of Flash Photonics, Inc., an affiliate Associate Professor at the University of Washington, and a consultant to the spectroscopy industry.

Direct correspondence to:

SpectroscopyEdit@ubm.com

For more information on this topic, please visit our homepage at: www.spectroscopyonline.com

Trusted brands. One company.

Newport® Ophir® Spectra-Physics®

MKS INSTRUMENTS, INC. • 978.645.5500 • WWW.MKSINST.COM

Determination of Rare Earth Elements in Geological and Agricultural Samples by ICP-OES

The selection of an analytical method featuring multielemental capability, wide linear range, and ease of operation would be ideal for rare earth element (REE) determination in complex samples. This work targets the determination of Ce, Dy, Er, Eu, Gd, Ho, La, Lu, Nd, Pr, Sc, Sm, Tb, Th, Tm, Y, and Yb in geological samples, fertilizer, and agricultural gypsum samples using inductively coupled plasma–optical emission spectrometry (ICP-OES). Samples were prepared using microwave-assisted acid digestion and the accuracy was evaluated by addition and recovery experiments for spiked samples at three concentration levels. A careful choice of the plasma viewing position and appropriate dilution factors led to accurate and sensitive determinations of REEs. The proposed procedure using external calibration presented good accuracy and sensitivity.

Clarice D. B. Amaral, Raquel C. Machado, Juan A. V. A. Barros, Alex Virgilio, Daniela Schiavo, Ana Rita A. Nogueira, and Joaquim A. Nóbrega

Rare earth elements (REEs) comprise the lanthanides series, as well as Sc and Y. Nowadays these elements are essential for high-technology and military applications (1), and some ores can be classified as a rich source of REEs, such as Ce, Dy, Er, Eu, Gd, Ho, La, Lu, Nd, Pr, Sc, Sm, Tb, Th, Tm, Y, and Yb. The most abundant REEs in the Earth's crust are Ce, La, Nd, and Y (31–66 $\mu\text{g/g}$), while Tm and Lu (0.5–0.8 $\mu\text{g/g}$) are found in lower contents (1,2).

The chemical analysis of REEs in geological materials is critical for better exploration of mineral reserves as well as for studies in geology and geochemistry because these elements present unique properties and can be used as geochemical tracers (3). Moreover, the predominant ionic form of some REEs is trivalent, which can replace Ca in phosphate minerals and may reach soil together with phosphorus fertilizers and agricultural gypsum (4,5).

Among the spectrochemical methods available, instrumental neutron activation analysis (INAA) and inductively coupled plasma–mass spectrometry (ICP-MS)

are commonly used for REE determination in mineral samples because of their multielement capability, high sensitivity, and low detection limits. However, these methods rely on expensive instrumentation and are prone to interferences caused by long irradiation times and spectral overlaps, respectively. In addition, X-ray fluorescence (XRF) spectroscopy may also be applied in the direct solid analysis of these samples; however, XRF lacks sensitivity and thus is not suitable for the determination of REEs at low concentrations (6). In this context, inductively coupled plasma–optical emission spectrometry (ICP-OES) has been reported in the literature as a feasible alternative for REE determination because of the multielement capacity, adequate sensitivity, wide linear dynamic range, and ease of operation (6–8).

Considering these aspects, the goal of this study was to evaluate the performance of ICP-OES for the determination of REEs in geological samples, phosphorus fertilizers, and agricultural gypsum samples. The ICP-OES instrument was evaluated for measurements in both radial view and dual view (axial and radial) modes.

Table I: Operational parameters for the ICP-OES system

Instrument Parameter	Operational Conditions
Read time (s)	20
Replicates	3
Sample uptake delay (s)	15
Stabilization time (s)	15
RF applied power (kW)	1.50
Argon auxiliary flow rate (L/min)	1.0
Argon plasma flow rate (L/min)	12.0
Argon nebulizer flow rate (L/min)	0.60
Viewing modes	Radial view and dual view
Sample uptake rate (mL/min)	1.0
Nebulizer	Seaspray
Nebulization chamber	Single-pass cyclonic

Table II: Background equivalent concentration (BEC) and LOD values obtained for radial and dual viewing modes

Radial View Mode			Dual View Mode		
Emission Wavelength (nm)	BEC (µg/L)	LOD (mg/kg)	Emission Wavelength (nm)	BEC (µg/L)	LOD (mg/kg)
Ce 418.659	10	1.9	Ce 418.659	0.1	0.1
Dy 353.171	9	1.1	Dy 340.780	0.7	0.6
Er 349.910	4	1.1	Er 369.265	0.08	0.1
Eu 397.197	0.4	0.09	Eu 397.197	3	2.6
Gd 336.224	3	0.6	Gd 335.048	1	0.5
Ho 341.644	8	0.9	Ho 339.895	0.9	0.8
La 379.477	1	0.2	La 408.671	0.7	0.5
Lu 307.760	3	0.7	Lu 307.760	0.5	0.4
Nd 406.108	40	2.8	Nd 401.224	2	1.0
Pr 422.532	9	1.8	Pr 422.532	0.08	0.02
Sc 363.074	0.5	0.2	Sc 335.372	0.05	0.05
Sm 360.949	8	2.7	Sm 360.949	2	1.3
Tb 367.636	10	1.7	Tb 350.914	0.6	0.7
Th 283.730	20	3.7	Th 283.730	3	1.6
Tm 342.508	3	0.9	Tm 346.220	0.08	0.08
Y 377.433	0.3	0.2	Y 371.029	30	0.8
Yb 369.419	0.5	0.1	Yb 289.138	3	1.6

Experimental Instrumentation

An ICP-OES system with a dichroic spectral combiner for simultaneous collection of data in radial and axial viewing mode was used to perform all measurements (5100 SVDV, Agilent Technologies). The instrument arrangement involves a vertical argon plasma. The plasma operating conditions and parameters of the sample introduction system are presented in Table I. Samples were prepared using microwave-assisted acid digestion with an Ethos 1 oven (Milestone).

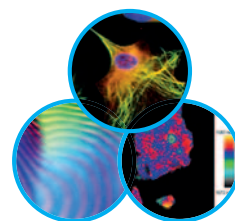
Reagents and Standard Solutions

All glassware was decontaminated by immersion in 10% v/v HNO₃ for at least 24 h and rinsed with distilled-deionized water (resistivity ≥ 18.2 MΩ-cm) obtained from a Milli-Q Water system (Millipore). All solutions and analytical blanks were prepared with ultra-pure water and nitric acid obtained using a sub-boiling distillation apparatus (Milestone). Concentrated nitric acid (65% m/m) and hydrochloric acid (37% m/m) were used to prepare the aqua regia solution used to digest samples. Analytical calibration solu-



See things clearer

with Cobolt



High Performance Lasers for Raman

- Single frequency
- UV-VIS-MIR
- CW & Q-switched
- Unprecedented reliability with HTCure™



Cobolt
a HÜBNER Group company

coboltlasers.com

tions in the 0.05–5 mg/L range were prepared by appropriate dilution of a multielement stock solution (Agilent Technologies) of 10 mg/L Ce, Dy, Er, Eu, Gd, Ho, La, Lu, Nd, Pr, Sc, Sm, Tb, Th, Tm, Y, and Yb. Limits of detection (LOD) were obtained by considering background equivalent concentrations

(BEC) and relative standard deviations (RSD) for 10 measurements of digested blank solutions.

Geological and Agricultural Samples Preparation

Approximately 100 mg of two geological samples (G1 and G2) were accu-

rately weighed directly in the PTFE-PFA digestion vessels, followed by the addition of 9.0 mL of aqua regia. The loosely capped vessels were left overnight for a predigestion step in a laminar flow clean hood. The digestion was further carried out in a closed-vessel microwave cavity oven according to the following three-step heating program: 10-min ramp to 120 °C, 20-min ramp to 220 °C, and a 5-min plateau at 220 °C. After the digests cooled to room temperature, they were transferred to previously decontaminated 50-mL polypropylene flasks and the volume was made up with distilled–deionized water. Seven fertilizer samples (A–G) and two agricultural gypsum samples (Gy1 and Gy2) were provided by Embrapa Pecuária Sudeste. Samples A, B, and C were a mixture of mineral fertilizers with different NPK contents with B, Cu, Mn, and Zn in their compositions. Samples D, E, and F were a mixture containing B, Cu, Mn, and Zn in a 20-fold higher concentration than samples A, B, and C. Sample G was an organomineral fertilizer. The fertilizer samples were submitted to a 2-h predigestion step at room temperature, followed by microwave-assisted digestion. Microwave-assisted digestions were performed by adding 6 mL of HNO₃

Table III: Addition and recovery experiments for REEs (mean ± standard deviation, $n = 3$) in fertilizer samples spiked at 0.1 and 1.0 mg/L for dual viewing mode

Emission Wavelength (nm)	Sample B		Sample D		Sample G	
	0.1 mg/L	1 mg/L	0.1 mg/L	1 mg/L	0.1 mg/L	1 mg/L
	Recovery (%)					
Ce 418.659	142 ± 9	94.9 ± 2	93.2 ± 0.2	107 ± 0.5	102 ± 1	99.2 ± 0.1
Dy 340.780	101 ± 1	95.8 ± 3	92.4 ± 0.1	101 ± 1	101 ± 0.2	100 ± 0.3
Er 349.91	99.2 ± 0.9	96.7 ± 0.7	90.9 ± 1	102 ± 0.9	107 ± 0.1	102 ± 0.5
Eu 397.197	108 ± 2	95.8 ± 1	91.7 ± 0.4	102 ± 2	100 ± 0.9	99.2 ± 1
Gd 342.246	107 ± 1	94.3 ± 0.2	98.4 ± 0.2	102 ± 3	98.4 ± 0.7	101 ± 0.2
Ho 389.094	107 ± 2	95.9 ± 0.4	99.2 ± 0.9	102 ± 0.8	107 ± 2	102 ± 0.9
La 408.671	158 ± 8	96.7 ± 1	91.7 ± 0.7	105 ± 0.2	100 ± 1	99.2 ± 0.7
Lu 261.541	101 ± 3	96.6 ± 0.6	101 ± 2	102 ± 0.2	109 ± 3	102 ± 0.1
Nd 410.945	82.0 ± 7	93.4 ± 0.7	107 ± 5	100 ± 1	90.2 ± 2	102 ± 1
Pr 390.843	123 ± 2	91.0 ± 1	90.2 ± 0.7	99.2 ± 2	90.2 ± 0.8	98.4 ± 0.6
Sc 363.074	109 ± 1	96.6 ± 0.2	92.4 ± 0.1	104 ± 4	101 ± 0.1	103 ± 0.2
Sm 359.259	104.8 ± 3	96.0 ± 0.9	88.7 ± 3	102 ± 0.3	105 ± 6	100 ± 0.5
Tb 367.636	96.0 ± 0.9	95.2 ± 0.5	88.0 ± 1	101 ± 0.1	104 ± 0.3	101 ± 0.7
Th 274.716	131 ± 2	93.4 ± 2	98.4 ± 0.7	110 ± 10	104 ± 0.7	106 ± 2
Tm 313.125	90.2 ± 5	94.3 ± 0.6	90.2 ± 0.2	101 ± 2	98.4 ± 0.1	101 ± 1
Y 360.074	118 ± 6	94.1 ± 0.4	101 ± 1	102 ± 1	109 ± 2	102 ± 0.3
Yb 289.138	96.0 ± 2	92.0 ± 0.3	96.0 ± 0.9	99.2 ± 0.5	104 ± 0.4	97.6 ± 1

Table IV: Determination of REEs (mean ± standard deviation, $n = 3$) in fertilizer and geological samples by ICP-OES with dual viewing mode

Emission Wavelength (nm)	Fertilizer A	Fertilizer B	Fertilizer C	Fertilizer D	Fertilizer E	Fertilizer F	Fertilizer G	Sample G1	Sample G2
	Determined (mg/kg)								
Ce 418.659	568 ± 41	665 ± 24	256 ± 3	122 ± 35	478 ± 7	283 ± 2	34 ± 3	16302 ± 1411	4092 ± 225
Dy 340.780	16 ± 2	21 ± 2	<0.6	<0.6	<0.6	<0.6	<0.6	60 ± 8	< 0.6
Er 349.91	8 ± 1	11 ± 1	<0.1	<0.1	10.00 ± 0.02	<0.1	<0.1	18 ± 4	< 0.1
Eu 397.197	<2.6	<2.6	<2.6	5.8 ± 0.5	20.00 ± 0.01	20.0 ± 0.2	<2.6	148 ± 11	58 ± 4
Gd 342.246	39 ± 3	46 ± 4	22 ± 2	11 ± 1	10.0 ± 0.3	14 ± 2	4.2 ± 0.5	330 ± 30	< 0.5
Ho 389.094	42 ± 3	49 ± 4	18 ± 2	10 ± 2	<0.8	<0.8	<0.8	< 0.8	< 0.8
La 408.671	289 ± 23	323 ± 10	128 ± 9	63 ± 19	229.0 ± 0.6	149 ± 2	14 ± 1	8005 ± 744	2798 ± 150
Nd 410.945	438 ± 30	466 ± 36	147 ± 11	197 ± 16	244 ± 5	152 ± 2	<1.0	6332 ± 592	1730 ± 96
Pr 390.843	169 ± 12	196 ± 6	<0.02	42 ± 9	33.30 ± 0.01	12.2 ± 2	12 ± 1	2160 ± 191	568 ± 30
Sc 363.074	35 ± 3	38 ± 4	<0.05	23 ± 2	<0.05	<0.05	<0.05	83 ± 8	153 ± 9
Sm 359.259	52 ± 4	63 ± 5	<1.3	11 ± 4	20.0 ± 0.3	10.0 ± 0.4	<1.3	513 ± 45	< 1.3
Tb 367.636	6.7 ± 0.7	9 ± 1	<0.7	<0.7	<0.7	<0.7	<0.7	155 ± 19	128 ± 8
Th 274.716	239 ± 17	288 ± 15	172 ± 8	252 ± 20	30.0 ± 0.1	50.0 ± 0.4	203 ± 4	345 ± 30	225 ± 13
Tm 342.508	< 0.08	< 0.08	< 0.08	< 0.08	< 0.08	< 0.08	< 0.08	35 ± 4	< 0.08
Y 360.074	88 ± 7	111 ± 4	<0.8	18 ± 4	20.00 ± 0.07	20.0 ± 0.1	5.8 ± 0.5	265 ± 26	80 ± 4
Yb 289.138	13 ± 1	14 ± 1	16 ± 1	<1.6	<1.6	<1.6	<1.6	20 ± 4	< 1.6

(7 mol/L) and 2 mL of H₂O₂ (30% w/w) to approximately 200 mg of sample. The heating program for fertilizer samples was implemented in two steps: a 20-min ramp to 220 °C, followed by a 20-min plateau at 220 °C. After the digested samples cooled down, they were transferred to polypropylene flasks and volumes were made up to 50.0 mL with distilled-deionized water. The accuracy of the proposed procedures was checked by addition and recovery experiments at a single level at 2.5 mg/L for geological samples and two concentration levels (0.1 and 1 mg/L) for fertilizers. Spikes were added before digestion to check the sample preparation step. Both digestion and recovery procedures were performed in triplicate for each sample.

Results and Discussion

Limits of Detection

The determination of REEs in geological samples, fertilizers, and agricultural gypsum was carried out using external calibration. Limits of detection were calculated considering BEC, signal-to-background ratio (SBR), and relative standard deviation (RSD) for 10 measurements of a blank solution, and the values are shown in Table II. Calibration curves with correlation coefficients better than 0.9990 were obtained for all analytes, showing the feasibility of the REE measurements by ICP-OES.

Eid and colleagues (9) reported LODs ranging from 0.009 to 0.45 mg/mL for eight REEs determined by ICP-OES in phosphate samples. Lichte and colleagues (10) described a procedure for the determination of REEs in geological materials by ICP-MS. The LODs were in the 2–11 ng/g range with precision (RSD) of 2.5%. However, spectral interferences had to be overcome, leading to the formation of oxides and promoting drifts in sensitivity.

Accuracy of the Procedure

Addition and recovery experiments were performed to check the accuracy of the proposed procedure. Samples of geological materials, fertilizers, and agricultural gypsum were spiked.

Geological sample G2 was spiked at 2.5 mg/L and the results demonstrated that suitable accuracies were attained in both viewings. Recoveries for all elements, except Ce, ranged from 90.1% to 107% for both viewing modes. The only exception was for Ce (418.659 nm), where recoveries presented a positive error, 110% and 118%, for radial and dual view modes, respectively. Applying a *t*-test, no statistical differences at a 95% confidence level were observed between the radial view and dual view modes. Lanthanum, Nd, and Pr were presented at high concentrations in both samples (G1 and G2), thus a fourfold additional dilution was necessary and reading in radial view mode was the best choice.

The REE concentrations in fertilizers were lower than in the geological samples; therefore spikes were added at lower levels in the fertilizer samples. Addition and recovery experiments (Table III) were applied to three fertilizer samples (B, D, and G) with different compositions. Due to the low REE concentrations in the fertilizers, the dual

viewing mode was used because of its higher sensitivity. The procedure presented suitable accuracy, except for Ce, La, Pr, Th, and Y at 0.1 mg/L in spiked sample B, because the concentrations of these REEs in sample B were higher than the spiked concentrations.

For the agricultural gypsum sample, spikes at 0.1 and 1.0 mg/L were performed. The best results were reached after a 10-fold additional dilution and using radial view configuration because of the higher concentrations of REEs in this sample, except for Ce, La, and Nd—the added concentrations for these elements were higher than the concentrations naturally present in the samples. Using the dual view mode, good accuracy was attained for lower level spikes (0.1 mg/L) except for Ce, La, and Nd; however, for spikes at the higher level (1.0 mg/L), recoveries were not satisfactory, because the added concentrations were too high when compared to the real concentrations in the sample. Thus, the careful choice of the viewing position and additional dilution led to proper accuracies and sensitivities for REE determination in both viewing modes. For agricultural gypsum samples, radial viewing mode was better.

Determination of REEs in Geological Samples, Fertilizer, and Agricultural Gypsum Samples

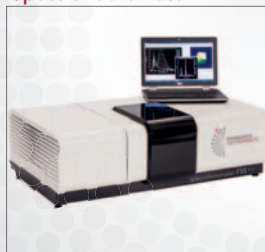
The developed procedure using dual view mode was applied to the determination of REEs in fertilizers and geological samples (Table IV). Geological sample 1 contained higher

EXPERTS in FLUORESCENCE SPECTROSCOPY



- > TIME-RESOLVED FLUORESCENCE
- > STEADY STATE FLUORESCENCE
- > PHOSPHORESCENCE LIFETIME
- > TRANSIENT ABSORPTION

FS5 Photon Counting
Spectrofluorometer



FLS1000 Photoluminescence
Spectrometer



Table V: Determination of rare earth elements (mean \pm standard deviation, $n = 3$) in agricultural gypsum samples by ICP-OES with radial viewing mode

Emission Wavelength (nm)	Gy1	Gy2
	Determined (mg/kg)	
Ce 446.021	3392 \pm 129	2197 \pm 62
Dy 340.780	24 \pm 1	33 \pm 3
Er 349.910	15.0 \pm 0.1	17.5 \pm 0.20
Eu 420.504	44 \pm 1	39 \pm 1
Gd 342.246	113 \pm 5	100 \pm 3
Ho 389.094	233 \pm 9	163 \pm 4
La 408.671	1585 \pm 69	1213 \pm 41
Lu 291.139	<0.7	2.50 \pm 0.02
Nd 401.224	1897 \pm 69	1338 \pm 35
Pr 422.532	316 \pm 13	223 \pm 7
Sc 361.383	5.00 \pm 0.08	2.50 \pm 0.06
Sm 360.949	116 \pm 16	103 \pm 3
Tb 367.636	17 \pm 3	20.0 \pm 0.2
Th 269.242	33 \pm 4	27.5 \pm 0.2
Tm 342.508	2.50 \pm 0.03	2.5 \pm 0.1
Y 371.029	89 \pm 1	125 \pm 3

concentrations of all the analytes than sample 2, except for Sc. Rare earth element determination by ICP-OES was fast and suitable recoveries were obtained. The addition and recovery experiments showed that spectral interferences were not an issue. Three emission lines for each of the 17 elements were measured in less than 2 min in both viewing modes and required a sample volume of approximately 3 mL, demonstrating a high sample throughput for the procedure. Some concentrated samples were further diluted before the analysis, which was not a problem considering the wide linear range of the calibration curves. In the agricultural gypsum samples, analytes were determined using the radial viewing mode (Table V).

Lutetium and Tm were not found in any fertilizer sample, and the REEs presented at higher concentration levels were the same as those previously cited by Tyler (2). Agricultural gypsum samples presented concentrations five-fold higher than those found in fertilizer samples.

Spectral and matrix interferences were reported by Eid and colleagues (9) for REE determination, where suppression in La II 408.6-nm and Nd II

406.1-nm emission intensities were observed because of high Ca concentrations. Jaron and colleagues (11) reported spectral interferences caused by Fe and Ti overlaps and matrix interferences caused by the presence of Ca and Mg during the analysis of geological samples. However, those interferences were not found in the present work. The ICP-OES method was fast and suitable for the determination of rare earth elements in a wide concentration range in geological and agricultural samples.

Conclusions

The ICP-OES method presented multi-element capability and selectivity that was compatible with accurate REE determination in complex materials such as ores and agricultural samples. The high sample throughput and adequate accuracy and precision of the developed procedure indicates that ICP-OES is a suitable alternative for REE determination in geological and fertilizer samples. The feasibility of fast measurements of emission signals in radial and dual viewing modes was demonstrated here.

The determination of REEs in geological and agricultural materials can provide valuable information about the geochemical formation, plant nutritional status, the need for supplementation, and possible contamination. Moreover, in some cases it is important to have a fast sample profile to check for possible interfering elements on other target analytes when applying different methods—for example, the magnitude of interferences caused by double-charged species of $^{150}\text{Sm}^{2+}$ and $^{150}\text{Nd}^{2+}$ on $^{75}\text{As}^+$ determination by ICP-MS (12).

Acknowledgments

The authors are grateful to grants 2013/26672-5 and 2014/18393-1 of São Paulo Research Foundation (FAPESP), for the scholarships provided to R.C.M. and A.V., and for research grant 2015/14488-0. The authors are also thankful to the Conselho Nacional de Desenvolvimento Científico e Tecnológico (CNPq, Grants 443771/2014-6 and 303107/2013-8), and Coordenação de Aperfeiçoamento de Pessoal de Nível Superior (CAPES – Grant 15/2104) for fellowships and financial support. We

also would like to thank Agilent Technologies for their support.

References

- (1) S. Al-Thyabat and P. Zhang, *Hydrometallurgy* **153**, 30–37 (2015).
- (2) G. Tyler, *Plant Soil*. **267**, 191–206 (2004).
- (3) K.H. Johannesson, K.J. Stetzenbachand, and V.F. Hodge, *Geochim. Cosmochim. Acta*. **61**, 3605–3618 (1997).
- (4) A. Bakou, C. Buser, G. Dandulakis, G. Brudvigand, and D.F. Ghanotakis, *Biochim. Biophys. Acta*. **1099**, 131–136 (1992).
- (5) C.H.R. Saueia, F.M. Le Bourlegat, B.P. Mazzilli, and D.I.T. Fávoro, *J. Radioanal. Nucl. Chem.* **297**, 189–195 (2013).
- (6) B. Zawisza, K. Pytlakowska, B. Feist, M. Polowniak, A. Kita, and R. Sitko, *J. Anal. At. Spectrom.* **26**, 2373–2390 (2011).
- (7) M.S. Navarro, H.H.G.J. Ulbrich, S. Andrade, and V.A. Janasi, *J. Alloy Compd.* **344**, 40–45 (2002).
- (8) A.K.G. Silva, J.C. de Lena, R.E.S. Froes, L.M. Costa, and C.C. Nascentes, *J. Braz. Chem. Soc.* **23**, 753–762 (2012).
- (9) M.A. Eid, J.A.C. Broekaert, and P. Tschöpel, *Fresenius J. Anal. Chem.* **342**, 107–112 (1992).
- (10) F.E. Lichte, A.L. Meier, and J.G. Crock, *Anal. Chem.* **59**, 1150–1157 (1987).
- (11) I. Jaron, B. Kudowska, and E. Bulska, *At. Spectrosc.* **21**, 105–110 (2000).
- (12) B.P. Jackson, A. Liba, and J. Nelson, *J. Anal. At. Spectrom.* **5**, 1179–1183 (2015).

Clarice D. B. Amaral and Raquel C. Machado are with the Group for Applied Instrumental Analysis in the Department of Chemistry at Federal University of São Carlos in São Carlos, Brazil and Embrapa Pecuária Sudeste in São Carlos, Brazil. **Juan A. V. A. Barros, Alex Virgilio, and Joaquim A. Nóbrega** are also with the Group for Applied Instrumental Analysis in the Department of Chemistry at Federal University of São Carlos. **Ana Rita A. Nogueira** is also with Embrapa Pecuária Sudeste. **Daniela Schiavo** is with Agilent Technologies in Barueri, Brazil. Direct correspondence to: clariceamaral@yahoo.com.br ■

For more information on this topic, please visit our homepage at: www.spectroscopyonline.com

CONNECT WITH SPECTROSCOPY ON SOCIAL MEDIA

Join your colleagues in conversation, respond to hot topic questions, and stay up-to-date on breaking news. "Like" and follow us on Twitter, LinkedIn, and Facebook today!



Spectroscopy[®]

Effective Removal of Isobaric Interferences on Strontium and Lead Using Triple-Quadrupole ICP-MS

Despite the numerous inherent advantages of using inductively coupled plasma–mass spectrometry (ICP-MS) as a tool for trace-elemental analysis, the removal of spectral interferences is still a concern for some applications, especially in metallurgical, environmental, and geological studies. Isobaric interferences such as ^{87}Rb on ^{87}Sr and ^{204}Hg on ^{204}Pb are difficult to remove even using high-resolution instruments. The use of reactive gases inside the ICP-MS collision–reaction cell (CRC) system may help to overcome such isobaric interferences, since isotopes of different elements may react differently and hence may differ in mass after a chemical reaction. To control unwanted side reactions, an additional mass-filtering quadrupole needs to be situated ahead of the collision–reaction cell, so that ions entering the cell can be controlled and unwanted side reactions can be avoided.

Daniel Kutscher, Simon Lofthouse, Simon Nelms, and Shona McSheehy Ducos

Unresolved spectral interferences may lead to biased results in inductively coupled plasma–mass spectrometry (ICP-MS). Single-quadrupole ICP-MS typically uses a comprehensive interference removal mechanism with an inert collision gas (helium) and kinetic energy discrimination (KED). This approach is based on the difference in size between an analyte and polyatomic interference and as such is effective for the removal of many common interferences. In some cases though, two elements may share isotopes with identical mass number. These isotope overlaps are commonly referred to in ICP-MS as *isobaric interferences*. As the elemental ions are of a similar size, KED is not able to resolve these interferences. In addition, as the difference in mass between overlapping isotopes is extremely low they cannot be spatially resolved using either quadrupole-based or high-resolution ICP-MS. Often, the correction of isobaric interferences is accomplished using mathematical methods; however, this

procedure may lead to increased measurement uncertainties. Isobaric interferences may be resolved using reactive gases (for example, O_2 or NH_3), in the cases where one element forms a different product ion to the other. However, side reactions may create new unwanted interferences with other ions extracted from a sample, so that full interference removal may not be possible. The use of oxygen as a reactive gas leads to product ions that are fairly easy to interpret (mass shifts of mainly 16, but also 17 and 18 amu), whereas using ammonia as a reactive gas leads to the formation of a wide variety of product ions, because different cluster ions will be formed for each individual isotope of a given element. With ammonia, mass shifts from as low as 15 amu are observed, but also product ions with over 100 amu mass differences can be formed. Interpreting results from unknown or complex sample matrices may therefore be challenging. Using triple-quadrupole ICP-MS, a dedicated mass filtering step ahead of the colli-

sion–reaction cell (CRC) system overcomes the problem of uncontrolled side reactions, because only ions with a mass-to-charge ratio similar to that of the analyte may enter the cell and subsequently react with gas molecules. In this work, the performance of quadrupole-based ICP-MS (using single- and triple-quadrupole operation modes) is evaluated for the removal of isobaric interferences.

Experimental

All measurements were accomplished using a Thermo Scientific iCAP TQ ICP-MS system (Thermo Fisher Scientific). The instrument was tuned daily using the auto-tune routines supplied with the operating software. All solutions were prepared gravimetrically from single-element standards. The precision of the isotope ratios was calculated from 10 main runs with 30 sweeps each. The data displayed in the following were not corrected for mass bias, so the isotope ratios may differ slightly from the true value. However, the effect of mass bias would affect all individual measurements in the same way, so that correction would not alter the fundamental findings. Generally, isotope ratios are noted together with the observed standard deviation (as an indication for the attainable precision of the measurement) throughout this work. Typically, the observed relative standard deviation of the isotope ratio was on the order of 0.1%. To compare the results obtained using conventional single-quadrupole ICP-MS analysis using kinetic energy discrimination (SQ-KED), single-quadrupole ICP-MS using reactive gases (SQ-O₂ and SQ-NH₃), and triple-quadrupole ICP-MS with mass filtering and use of reactive gases (TQ-O₂ and TQ-NH₃), the ICP-MS system was configured to scan all samples in the three corresponding measurement modes. An overview of the instrument's settings can be found in Table I.

Results and Discussion

Two prominent examples for isobaric interferences are the detection of ⁸⁷Sr (7.00% abundant in nature) in the presence of Rb, which also has an isotope with mass number 87 (⁸⁷Rb is 27.84% abundant). Secondly, ²⁰⁴Pb (1.40% abundant) is interfered by ²⁰⁴Hg (6.85% abundant), which is of special concern for geological applications, where the ²⁰⁴Pb isotope is often used as a reference isotope (because it is not affected by radioactive decay of U or Th).

Using single-quadrupole ICP-MS, strontium is typically analyzed using kinetic energy discrimination to make sure polyatomic interferences are removed, but also use of the standard mode (no interference removal) may be feasible depending on the sample. For removal of the isobaric interference of ⁸⁷Rb, oxygen can be used as a reactive gas in the CRC system. Whereas Sr undergoes an oxidation reaction and hence forms product ions with *m/z* 103 (⁸⁷Sr¹⁶O⁺) and 104 (⁸⁸Sr¹⁶O⁺) respectively, ⁸⁷Rb does not react with oxygen. If the analyzing quadrupole of either a single- or triple-quadrupole ICP-MS system is set to scan *m/z* 103 and 104 under these conditions,

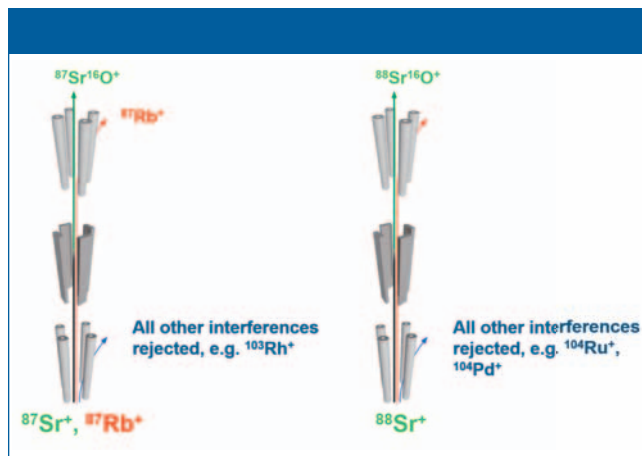


Figure 1: Schematic illustrating the analysis of strontium isotopes in presence of Rb using triple-quadrupole ICP-MS operated with oxygen as reaction gas.

only Sr will be detected. However, only triple-quadrupole instruments can filter out ions potentially interfering at the new product ion mass of Sr, such as ¹⁰³Rh⁺, ¹⁰⁴Ru⁺, or ¹⁰⁴Pd⁺. Figure 1 shows how all quadrupoles need to be set to scan for this application.

To evaluate the performance in different measurement modes for Sr, a calibration curve was acquired using SQ-KED as a reference, and using triple-quadrupole MS in combination with oxygen as a reactive gas. The result-

Starna
'Setting the Standard'

Starna Cells
Quality others strive to match

By joining optical surfaces by heat fusion alone, Starna revolutionised cell quality and performance.

Vast, competitively priced range for every application

Custom design and manufacture for anything else!

Starna Cells Inc.
(800) 228-4482
sales@starnacells.com
www.starnacells.com

Table I: Instrumental parameters			
Parameter	Value		
Nebulizer	MicroMist quartz nebulizer 0.4 mL/min, pumped at 40 rpm		
Spray chamber	Quartz cyclonic spray chamber cooled at 2.7 °C		
Injector	2.5 mm i.d., quartz		
Interface	High sensitivity (2.8 mm) insert, Ni cones		
RF power	1550 W		
Nebulizer gas flow	1.11 L/min		
QCell Settings	SQ-KED	SQ-O ₂ , TQ-O ₂	SQ-NH ₃ , TQ-NH ₃
Gas flow	100% He, 4.5 mL/min	100% O ₂ , 0.35 mL/min	100% NH ₃ , 0.33 mL/min
CR bias	-21 V	-7.5 V	-7.5 V
Q3 bias	-18 V	-12 V	-12 V
Scan settings	0.1 s dwell time per analyte, 30 sweeps, 10 main runs		

Table II: Isotope ratio for ⁸⁸ Sr/ ⁸⁷ Sr in solutions containing varying amounts of Rb			
Sample	Measured Isotope Ratio ⁸⁸ Sr ¹⁶ O/ ⁸⁷ Sr ¹⁶ O Using TQ-O ₂ Mode*	Measured Isotope Ratio ⁸⁸ Sr/ ⁸⁷ Sr Using SQ-KED Mode*	Measured Isotope Ratio ⁸⁸ Sr ¹⁶ O/ ⁸⁷ Sr ¹⁶ O Using SQ-O ₂ Mode*
10 µg/L Sr	12.1175 ± 0.1447	12.6280 ± 0.1097	9.0228 ± 0.0550
10 µg/L Sr, 10 µg/L Rb	12.0635 ± 0.0877	2.6572 ± 0.0122	N/A
10 µg/L Sr, 100 µg/L Rb	12.1053 ± 0.1123	0.3216 ± 0.0158	N/A
10 µg/L Sr, 1 mg/L Rb	12.1183 ± 0.1160	0.0311 ± 0.0003	N/A
10 µg/L Sr, 10 mg/L Rb	12.0741 ± 0.0907	0.0032 ± 0.00004	N/A
10 µg/L Sr, 10 mg/L Rb, 1 mg/L Rh	12.0464 ± 0.0970	2.5832 ± 0.0157	0.0038 ± 0.000005
10 µg/L Sr, 10 mg/L Rb, 10 mg/L Ru	12.1338 ± 0.1094	2.5992 ± 0.0205	10634. ± 848
10 µg/L Sr, 10 mg/L Rb, 1 mg/L Rh; 10 mg/L Ru	12.0003 ± 0.1074	2.6338 ± 0.0158	2.0209 ± 0.0059

*No mass bias correction applied

Table III: Isotope ratio for ²⁰⁴ Pb/ ²⁰⁸ Pb in solutions containing varying amounts of Hg and Yb			
Sample	Measured Isotope Ratio ²⁰⁴ Pb/ ²⁰⁸ Pb Using SQ-KED*	Measured Isotope Ratio ²⁰⁴ Pb/ ²⁰⁸ Pb Using SQ-NH ₃ *	Measured Isotope Ratio ²⁰⁴ Pb/ ²⁰⁸ Pb Using TQ-NH ₃ *
1 µg/L Pb µg/L	0.0258 ± 0.0001	0.0258 ± 0.0001	0.02581 ± 0.0001
1 µg/L Pb + 5 µg/L Hg	0.4301 ± 0.0025	0.0258 ± 0.0001	0.02591 ± 0.0001
1 µg/L Pb + 10 µg/L Hg	0.8941 ± 0.0055	0.0258 ± 0.0001	0.02589 ± 0.0001
1 µg/L Pb + 20 µg/L Hg	1.8270 ± 0.0051	0.0258 ± 0.0001	0.02589 ± 0.0001
1 µg/L Pb + 1 mg/L Yb	0.0469 ± 0.0011	0.0721 ± 0.0002	0.02592 ± 0.0001

*No mass bias correction applied

ing detection sensitivity using oxygen and a mass shift reaction was about 30% in comparison to SQ-KED (14 kcps/µg/L in comparison to 51 kcps/µg/L); however, the instrumental detection limit was not affected (0.001 µg/L for ⁸⁸Sr in both modes of analysis).

In a second experiment, solutions containing 10 µg/L and varying concentrations of Rb were analyzed and the isotope ratio ⁸⁸Sr/⁸⁷Sr was evaluated. Furthermore, solutions containing equal amounts of Sr and Rb in a matrix containing either or both 1 mg/L of Pd and 10 mg/L of Ru (to

account for the lower abundance of the ¹⁰⁴Ru isotope in comparison to monoisotopic ¹⁰³Rh) were analyzed. Typically, considering the isotopic abundance of the strontium isotopes ⁸⁷Sr and ⁸⁸Sr, one would expect a theoretical isotope ratio of 11.7971. The results are displayed in Table II.

As can be seen from Table II, the increasing amount of Rb (and hence the abundance of ions with *m/z* 87) has no effect on the Sr isotope ratio when using the TQ-O₂ mode. In contrast, the single-quadrupole approach using KED reveals a strong effect of the increasing amount of Rb in the sample solution, because the isobaric interference is not resolved. When using oxygen as a reactive gas in single-quadrupole ICP-MS analysis, the obtained isotope ratio is mainly determined by the interfering ions on the product ion mass of ^{87,88}Sr¹⁶O, which are not removed and remain occupied, since neither Rh nor Ru react with oxygen. Even the observed isotope ratio for a solution containing only Sr is strongly biased by other ions of unknown identity formed in the cell.

For Pb, similar experiments were conducted to estimate the effect of the isobaric interference caused by ²⁰⁴Hg on ²⁰⁴Pb. To judge how far the isobaric interference was eliminated, the isotope ratio ²⁰⁴Pb/²⁰⁸Pb (reference value 0.02672) was used as a reference.

For elimination of the isobaric interference from Hg on Pb, a reaction with ammonia can be used. Hg undergoes a chemical reaction with ammonia molecules and forms product ions that have a different *m/z* value. At the same time, Pb does not react with ammonia, so it can be detected free from interferences when the analyzing quadrupole (Q3) is set to the same mass as the first quadrupole (that is, mass 204 in this case). It is therefore important to avoid other reactions in the cell that could lead to the formation of a product ion with *m/z* 204, so lower mass ions that could generate additional interferences need to be removed in the first quadrupole. Again, the objec-

tive was to investigate how far traditional single-quadrupole approaches in comparison to triple-quadrupole operation may be suitable for this application. For the single-quadrupole mode tests, ammonia was also used as the reactive gas, but with Q1 acting as an ion guide only, so that other ions also originating from the sample could enter the CRC system.

Table III clearly shows that, again, KED does not enable the removal of isobaric interferences, as the measured isotope ratio changes with increasing concentration of Hg added to the solution. In contrast, the use of NH_3 as a reactive gas in single-quadrupole mode is capable of eliminating the isobaric ^{204}Hg interference from ^{204}Pb . Because no other ions are present in the ion beam when analyzing a solution containing only Hg and Pb, the use of an additional mass filter or of Q1 as an ion guide is unnecessary. However, for real sample analysis this situation is almost never the case. If for example rare-earth elements are present in the sample solution (which is likely in geological samples such as soils or rock digests), other cluster ions may be formed with NH_3 , so that m/z 204 is again interfered. To test this phenomenon, 1 mg/L of ytterbium was added to the measured solution to introduce $^{170}\text{Yb}(\text{NH}_3)_2$ as a potential interference on ^{204}Pb in SQ- NH_3 mode. Again, a biased $^{204}\text{Pb}/^{208}\text{Pb}$ isotope ratio is observed, clearly showing that there is an effect from $^{170}\text{Yb}(\text{NH}_3)_2$ interference on ^{204}Pb in SQ- NH_3 mode. To visualize this newly formed polyatomic interference, a full mass spectrum was acquired using NH_3 as reactive gas (Figure 2).

It can be seen that there are numerous cluster molecules formed from Yb and NH_3 . Although unreacted Yb still shows the highest abundance in the mass spectrum between m/z 168 and 176 (indicating that the reaction is not quantitative), the characteristic isotope pattern for Yb can also be repeatedly found at higher mass, with an equal distance of 17 amu between corresponding isotopes. This mass difference reveals the successive addition of one molecule of NH_3 per precursor ion

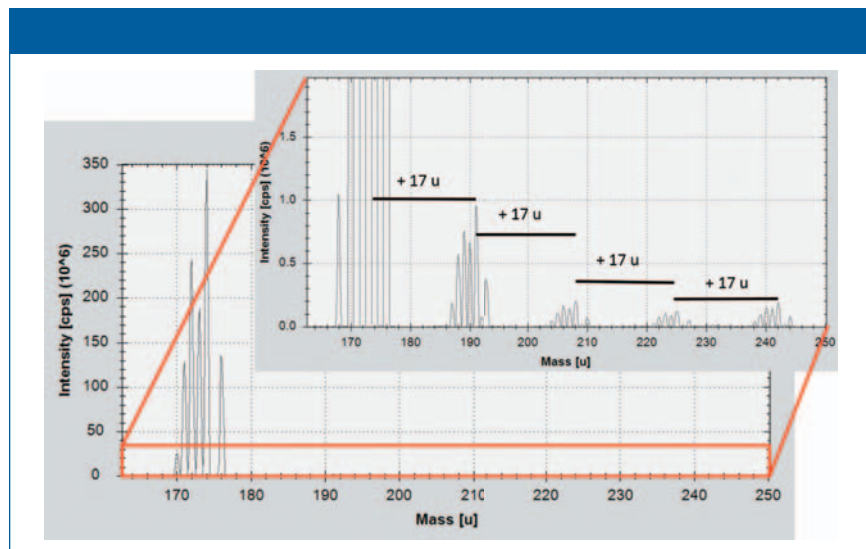


Figure 2: Full mass spectrum illustrating the formation of Yb-derived product ions acquired using single-quadrupole operation and ammonia as reaction gas.

and is characteristic for reactions of this gas. The main interference now found on m/z 204 corresponds to $^{170}\text{Yb}(\text{NH}_3)_2^+$, but since all seven Yb isotopes react in the same way, the other Pb isotopes would also be similarly interfered. In SQ- NH_3 mode, these newly formed polyatomic ions are transmitted with the isotope mass of interest and therefore introduce a new interference on the target isotope. In contrast, when switching to a triple quadrupole-based measurement mode (TQ- NH_3), all other ions with lower mass (such as ^{170}Yb) are removed from the ion beam before they enter the CRC system and are not able to generate these new interferences. The side reaction of Yb with NH_3 therefore does not lead to the formation of new interferences on Pb, and in turn, the $^{204}\text{Pb}/^{208}\text{Pb}$ measured isotope ratio is not affected at all through the presence of either Hg or Yb. Furthermore, other rare-earth elements that may lead to the formation of new interferences on ^{204}Pb because of their reactivity toward ammonia—for example, cerium ($^{136}\text{Ce}[\text{NH}_3]_4^+$, 0.19% abundant) or europium ($^{153}\text{Eu}[\text{NH}_3]_3^+$, 52.20% abundant)—are also removed by Q1 in triple-quadrupole mode.

Conclusion

The removal of isobaric interferences using reactive gases has been dem-

onstrated in two examples, ^{87}Rb on ^{87}Sr and ^{204}Hg on ^{204}Pb . Leveraging different reactivity toward oxygen and ammonia, respectively, allows a chemical separation of the isobars inside the CRC system. Although single-quadrupole instruments are also capable of using reactive gases, unwanted side reactions with other elements present in the sample may lead to the formation of new interferences, as has been shown in the case of Yb and Pb. The importance of controlling the ions entering the CRC is a key factor with respect to obtaining analytical accuracy. Triple-quadrupole ICP-MS using a dedicated mass filter in front of the CRC system is the only definitive way of achieving this required ion transmission control.

Daniel Kutscher and Shona McSheehy Ducos are with Thermo Fisher Scientific in Bremen, Germany. **Simon Lofthouse and Simon Nelms** are with Thermo Fisher Scientific in Stafford House, Hemel Hempstead, UK. Direct correspondence to: daniel.kutscher@thermofisher.com ■

For more information on this topic, please visit our homepage at: www.spectroscopyonline.com

Tandem LA–LIBS Coupled to ICP–MS for Comprehensive Analysis of Tumor Samples

Elemental imaging is regarded as a valuable approach for a wide application range in modern medicine. Using tandem laser-ablation laser-induced breakdown spectroscopy (LA–LIBS) coupled to inductively coupled plasma–mass spectrometry (ICP–MS), high-sensitivity detection of trace metals can be combined with the possibility of analyzing nonmetallic bulk components of biological samples (for example, carbon, hydrogen, and oxygen). In this work, the applicability of the tandem LA–LIBS approach for the laterally resolved elemental analysis of a mouse model tumor sample after administering cytostatic medication is demonstrated. Results show that trace elements can be detected using the LA–ICP–MS domain of the setup while major components of the samples are analyzed simultaneously using LIBS. By expanding the analyte range covered during one analysis, information could be extracted from the data set that is not accessible to either of the stand-alone analysis methods.

Maximilian Bonta, Szilvia Török, Balazs Döme, and Andreas Limbeck

Laser-ablation inductively coupled plasma–mass spectrometry (LA–ICP–MS) is accepted nowadays as one of the prime methods for trace-element imaging in biological samples (1,2). The method's excellent limits of detection below the microgram-per-gram range for most elements paired with a wide dynamic range and a number of valid approaches for quantification make this method the perfect choice when trace-element distributions need to be assessed (3). Thereby, endogenous elements (4,5) as well as analytes originating from external sources (for example, drug administration) have already been analyzed (6,7). During the past few years, more-sophisticated quantification strategies have successfully been developed to allow simpler and more accurate analysis (8,9). Achievable lateral resolutions are descending toward the low micrometer range and below (10,11), driven by the development of ultrafast washout cells (12,13). However, one weakness of LA–ICP–MS remains: the possibility to analyze nonmetals, especially those present in biological samples. Although the analysis of phosphorus is rather unproblematic, investigations of sulfur and carbon are already more complicated: They are severely influenced by spectral interferences

(for example, $^{32}\text{S}^+ - ^{16}\text{O}^{16}\text{O}^+$, $^{34}\text{S}^+ - ^{16}\text{O}^{18}\text{O}^+$). In particular for carbon, the high first ionization potential is also a problem. When aiming to detect hydrogen, oxygen, or nitrogen using LA–ICP–MS, the analysis will not be successful at all because of the high background signals and weak ionization of these analytes in the Ar plasma. Thus, alternative methods are necessary if analysis of the biological bulk elements is desired.

In contrast to LA–ICP–MS, laser-induced breakdown spectroscopy (LIBS) is a technique far less commonly used for imaging studies on biological tissues (14,15). Although the limits of detection for metallic analytes are usually higher compared to LA–ICP–MS, the method provides the possibility to detect biological bulk elements such as carbon, hydrogen, and oxygen with sufficient sensitivity. A combination of both techniques is realized in so-called tandem LA–LIBS systems, which, when coupled to ICP–MS for analyte detection, extract the benefits of both the stand-alone methods described above (16,17). When irradiating the sample surface with a short-pulse laser beam, the light emitted by the laser-induced plasma is collected and analyzed by optical means—the LIBS domain of the system. In parallel, the generated sample aero-

sol is transferred to an ICP-MS system, like in regular LA-ICP-MS analysis. Such multimodal chemical imaging approaches, where two or more methods are used to analyze the same sample, have already been shown to deliver insightful results for biological questions. For example, the combination of LA-ICP-MS and organic mass spectrometry (such as matrix-assisted laser desorption–ionization mass spectrometry [MALDI-MS]) can deliver molecular as well as elemental distribution information from one specimen (18).

In this study, tandem LA-LIBS coupled to ICP-MS has been used for multimodal elemental mapping of a tumor sample obtained from a mouse model. The specimen underwent a combination treatment with two cytostatic drugs, sunitinib and cisplatin, with the aim to increase drug efficacy. The use of such a hybrid analysis approach could provide a complete elemental analysis of tissue samples including trace and minor elements as well as bulk elements in biological samples. Because of the excellent sensitivity of LA-ICP-MS, platinum originating from the administered drug could also be detected in the tissue. Within this study, it could be shown that gaining information about the bulk element distributions can essentially increase the value of elemental imaging studies.

Experimental

Animal Experiments and Sample Preparation

The C26 mouse colon adenocarcinoma cell line (Cell Line Service, Mason Research Institute) was cultured in Roswell Park Memorial Institute (RPMI) 1640 medium with 10% fetal bovine serum and 1% penicillin–streptomycin (all from Sigma Aldrich) in a humidified atmosphere at 37 °C, 5% CO₂. Groups of six 8-week-old female Balb/C mice from the colony of the National Oncology Institute in Budapest were inoculated subcutaneously with 2 × 10⁶ C26 cells.

All animal-model protocols were developed and conducted in accordance with the Animal Research: Reporting of In Vivo Experiments (ARRIVE) guidelines and the animal welfare regulations of the Department of Tumor

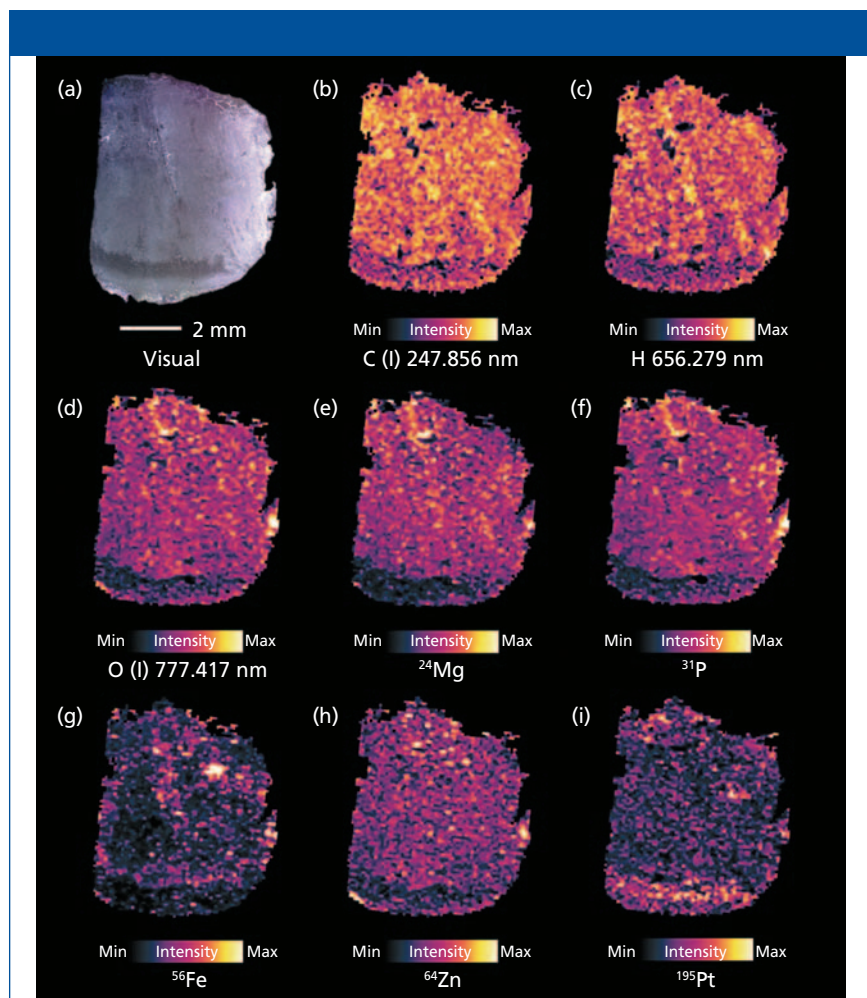


Figure 1: Compilation of selected elemental distributions measured on an adenocarcinoma sample using tandem LA-LIBS coupled to ICP-MS. Shown are (a) a microscopic image of the sample alongside the distributions of (b) carbon, (c) hydrogen, and (d) oxygen measured by LIBS (background corrected signal intensities), and (e) magnesium, (f) phosphorus, (g) iron, (h) zinc, and (i) platinum detected by LA-ICP-MS (gold-normalized signal intensities).

Biology, National Koranyi Institute of Pulmonology (permission number: 22.1/1268/3/2010). Mice were kept on a daily 12-h light/12-h dark cycle and held in a conventional animal house in microisolator cages with water and laboratory chow ad libitum.

Sunitinib was purchased from LC Laboratories (CAS. No. 557795-19-4) at >99% purity and suspended in 2% carboxymethylcellulose with 2-mg/mL methyl-4 hydroxybenzoate (both from Sigma Aldrich). Cisplatin was purchased from Accord Healthcare (Ma No.: OGYI-T-21728/01).

Sunitinib treatment began seven days after tumor cell injection and was performed orally with a feeding tube once daily at a dose of 80 mg/kg each day for two weeks. With the final dosage of

sunitinib, mice also received a bolus of cisplatin intraperitoneally at a dose of 10 mg/kg. The animals were sacrificed 3 h after the last treatment. Tumors were removed and snap frozen by submerging the tissues into dry ice-cooled isopentane. Frozen tissues were stored at -80 °C until utilization.

Cryo-cut sections of tumor tissue with a thickness of 10 μm were deposited onto silicon wafers. Silicon substrates were surface modified with (3-aminopropyl)triethoxysilane (APES) to optimize adhesion of the tissue section according to a protocol used in a previous study (19). Before analysis, the samples were coated with a thin gold layer to be used as a pseudo-internal standard during LA-ICP-MS data acquisition. For coating, an Agar B7340 sputter coater

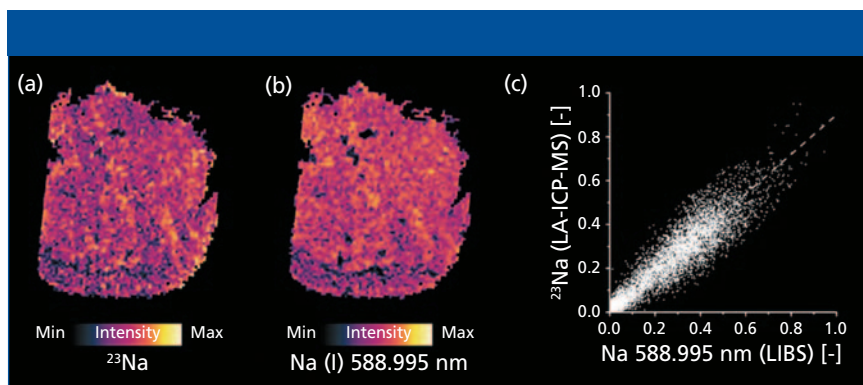


Figure 2: Distributions of sodium measured by (a) LA-ICP-MS and (b) LIBS. Signal intensities are normalized to 1 with regards to the highest signal detected over the complete sample; good correlation of the two modalities is demonstrated by (c) a pixel-by-pixel regression.

(Agar Scientific Limited) equipped with a gold sputter target was used. Samples were sputtered for 10 s (timer controlled) at a pressure of 0.1 mbar with a constant distance of 3.0 cm between sputter target and sample. This procedure has already been reported earlier to be suitable for signal normalization in LA-ICP-MS imaging (20).

Sample Analysis

Tandem LA-LIBS experiments were performed using a commercially available J200 tandem LA-LIBS system (Applied Spectra, Inc.) equipped with a frequency quadrupled Nd:YAG laser operating at a wavelength of 266 nm. Element-specific radiation emitted from the laser-induced plasma was collected by optical fibers and analyzed using a Czerny-Turner-type spectrometer with six-channel charge-coupled device (CCD) detection. This setup enabled the analysis of the full spectral range between 190 and 1050 nm (spectral resolution approximately 0.1 nm) for every laser shot. Axiom software provided by the manufacturer of the instrument was used for collection of the LIBS data. The system was connected to an iCAP Qc ICP-MS system (Thermo Fisher Scientific) using polytetrafluoroethylene (PTFE) tubing with a 3-mm inner diameter and a length of 1.5 m. A helium flow rate of 0.9 L/min provided optimal washout properties for the sample aerosol, and 0.3 L/min argon was admixed to the helium flow directly after the ablation chamber as make-up gas. ICP-MS data were acquired in time-resolved mode using Qtegra software provided

by the manufacturer of the system. Instrumental parameters of the LIBS system were optimized in preliminary experiments: Cryo-cuts of homogenized tissue samples were ablated and the parameters (that is, laser output energy and spectrometer gate delay) were selected to detect the maximum background corrected signal for carbon at the analytical wavelength of 247.856 nm, because the carbon signal was the weakest of all analytes aimed to be analyzed by LIBS. Before every analysis, instrumental parameters of the ICP-MS system were optimized by ablating the National Institute of Standards and Technology (NIST) 612 certified reference material (trace elements in glass) with the optimized laser settings for the LIBS domain. Settings were tuned to achieve the maximum signal intensity for ^{23}Na , ^{56}Fe , and ^{63}Cu ; typical instrumental parameters are shown in Table I.

Samples were ablated using parallel line scans without spacing between consecutive lines; all lines were scanned in the same direction. Stage scan speed was adjusted to traverse the complete diameter of the laser beam between two adjacent laser shots. The complete sample was ablated in one run of analysis. Settings were adjusted to obtain a lateral resolution of 60 μm per pixel for the final elemental distribution images obtained by both LIBS and LA-ICP-MS.

Image Construction and Coregistration

The acquired time-dependent intensity plots by LA-ICP-MS were transformed into elemental distribution images using

ImageLab software (v1.98, Epina GmbH) and raw data were normalized by the recorded gold signal. The LIBS dataset, where each spectrum corresponds to one discrete position on the sample, was analyzed using Aurora software (v.18, Applied Spectra, Inc.). After integration and background correction of selected analyte signals, two-dimensional (2D) maps were exported to ImageLab for further data processing. Using the known spatial coordinates of features and the measured sample area, the distribution images from the two analysis modes could be coregistered along with a microscopic image of the sample taken before ablation.

Results

Elemental Mapping of an Adenocarcinoma Tumor Sample

An approximately 5 mm \times 5 mm large mouse model adenocarcinoma tumor sample (10 μm thickness) treated with the anticancer drugs cisplatin and sunitinib was investigated in this study. A 60- μm lateral resolution of the elemental distribution images was sufficient for reliable interpretation of the results and keeping analysis time as low as possible. Analysis of the shown sample required around 1.5 h, which is also acceptable for measurements of a larger sample pool.

Using the LIBS domain of the setup, analysis of the biological bulk elements carbon, hydrogen, and oxygen was feasible. Additionally, alkaline and earth alkaline metals usually occurring at elevated concentrations in biological systems (that is, Na, K, Mg, and Ca) could be well detected using this technique. Signals of the strongest emission lines of those elements were well above background level on all areas of the sample with a signal-to-noise ratio always above 5.0. The silicon sample carrier exhibited no significant background signals for the investigated emission lines. Average background corrected signal intensities ranged from 2000 cts for C to 50,000 cts for Na. Elements occurring at lower concentrations were analyzed using the LA-ICP-MS modality of the setup. Namely, those were phosphorus and sulfur alongside with endogenous trace metals (such as Fe, Cu, Zn) and platinum originating from cisplatin treatment of

the mouse. Also for these elements, the silicon carriers did not exhibit significant background signals, which allowed sensitive detection. With average signal intensities ranging between 5000 cts for Pt and 200,000 cts for P, all elements of interest could be clearly detected above background level. A compilation of the elements detected by the two modalities is shown in Table II.

Using the earlier described procedure, elemental distribution images from the two modalities were combined. Selected elemental maps are shown in Figure 1. While the bulk elements carbon (Figure 1b) and hydrogen (Figure 1c) show rather homogenous distribution, oxygen (Figure 1d) and phosphorus (Figure 1f) are not evenly distributed across the sample. A reduced intensity can be seen in the bottom area of the sample. Magnesium (Figure 1e) and zinc (Figure 1h) follow a similar pattern. Sodium, as well as potassium (not shown) are again rather evenly distributed across the tissue sample. Compared to a tendency of depletion in the distinct bottom part of the sample for some elements, the platinum signal is elevated in this area.

Discussion

Comparison of Elemental Maps Derived From LIBS and LA-ICP-MS Measurements

Some elements (see Table II) could be detected using both modalities of the measurement system. Optimally, the two obtained elemental distributions should deliver the same result—a requirement for reliable results. Localization of corresponding pixels as well as relative signal intensities should correlate well. Besides a visual comparison (Figures 2a and 2b), linear correlation of corresponding pixels is also a simple tool for determining similarity and spatial matching of two images (Figure 2c).

As an example, the detected Na distributions are examined here. When visually comparing the elemental distributions measured simultaneously by LIBS and LA-ICP-MS, a good correlation is already expected. The shape of the tissue sample as well as the fine structures represented by varying relative signal intensities match well. This finding is underlined by the determina-

Table I: Summary of the instrumental parameters for the tandem LA-LIBS measurements

Laser-Ablation System	
Laser output energy (mJ)	13.2
Laser-ablation crater (μm)	60
Laser repetition rate (Hz)	2
Stage scan speed ($\mu\text{m/s}$)	120
Carrier gas flow (He) (L/min)	0.9
Make-up gas flow (Ar) (L/min)	0.3
Spectrometer System (Czerny-Turner type)	
Detection channels	6
Detector	CCD
Gate delay (μs)	0.1
Gate width (ms)	1.05
ICP-MS System	
Cool gas flow (Ar) (L/min)	15.0
Auxiliary gas flow (Ar) (L/min)	0.8
RF power (W)	1550
Dwell time per isotope (ms)	10
Cone system	Ni
Measured isotopes	^{13}C , ^{23}Na , ^{24}Mg , ^{25}Mg , ^{31}P , ^{32}S , ^{39}K , ^{42}Ca , ^{44}Ca , ^{56}Fe , ^{57}Fe , ^{63}Cu , ^{65}Cu , ^{64}Zn , ^{68}Zn , ^{194}Pt , ^{195}Pt , ^{197}Au

Table II: Compilation of the detected analytes

	C	H	O	P	S	Na	K	Mg	Ca	Fe	Cu	Zn	Pt
LA-ICP-MS	✓	—	—	✓	✓	✓	✓	✓	✓	✓	✓	✓	✓
LIBS	✓	✓	✓	—	—	✓	✓	✓	✓	—	—	—	—

tion of the image similarity using linear correlation. The high numerical value of the Pearson's correlation coefficient ($R = 0.918$) and normally distributed residuals from the linear fitting function (Kolmogorov-Smirnov test, $\alpha = 0.99$) do not indicate a significant difference between the two distribution images, neither from their positioning nor their relative signal intensities. Comparable findings can be reported for the other elements detected using both modalities. The high similarity of all simultaneously detected analytes demonstrates the viability of this multimodal elemental imaging approach. The combined data set thus offers valid information about the measured analyte distributions.

Apoptosis in Adenocarcinoma Samples

The most significant area in the micro-

scopic image, as well as the elemental distribution images, is the bottom area of the tissue sample (Figure 1). Histological stainings of consecutive thin-cuts show that the area in the microscopic image that appears slightly darker than the rest of the sample represents an apoptotic part of the tumor (Figure 1a). Here, signal intensities of phosphorus, oxygen, and also metals are significantly reduced in comparison to the remaining tissue section. This result is interesting because it shows a good correlation of the phosphorus (LA-ICP-MS) and oxygen distributions (LIBS). This finding points toward the fact that the abundance of phosphate is reduced in the apoptotic area compared to the rest of the sample. Such a finding is well explained by the processes occurring during apoptosis, which is a stage of a cell's life cycle also

known as *programmed cell death* (21). At the beginning of this phase, cellular functions are down-regulated leading to decreased metabolic activity, which is linked to the presence of phosphates in different forms: Adenosinotriphosphate (ATP) and its derivatives, as well as desoxyribonucleic acid (DNA) and ribonucleic acid (RNA) are just a few examples. Thus, lower phosphate content in apoptotic areas can be expected. Similar findings can be reported for physiologically relevant (trace-level) metals, such as magnesium or zinc, which also play a major role for proper enzyme functioning (22,23). Apoptosis is most likely induced by the treatment using sunitinib, which should inhibit cellular signaling by targeting multiple receptor tyrosine kinases (RTKs). Conversely, elevated concentrations of platinum, originating from the cisplatin treatment, can be found in the apoptotic tissue area. Possible resistance mechanisms that can lead to drug removal from the tumor sites are impaired in the apoptotic state, leading to a more efficient impact of the drug in such combinational treatment. Compared to the above described elements, bulk elements like carbon and hydrogen show rather uniform distribution, indicating similar composition and density of the tissue across the complete investigated sample.

Conclusion

In the past, trace-metal mapping in biological tissues has already been shown to provide valuable results for further medical interpretation. Deeper knowledge of the function of metals in tissues is believed to be able to provide valuable insight into complex biological processes, such as tumor genesis and drug efficacy. With additional information on biological bulk elements, the value of elemental imaging in the life sciences can be further expanded, as shown in the present example for tumor imaging. Not only can the information depth of LA-ICP-MS imaging be expanded by adding the LIBS domain, but because of the simultaneous measurement of a full spectrum with every laser shot, the analytes do not have to be selected before analysis as is usual with quadrupole ICP-MS instrumentation. This advantage gives the possibility

of mapping all elements that can be detected without jeopardizing the quality of the measured results. Additionally, the number of elements monitored using LA-ICP-MS can be reduced, leading to shorter cycling times and a longer data acquisition time for low-concentration elements. In further studies, tandem LA-LIBS coupled to ICP-MS can be used for quantitative imaging applications and for answering deeper medical questions.

The findings described above illustrate the excellent suitability of tandem LA-LIBS imaging for biological applications. Using the exceptional features of such a multimodal approach it was possible to map both bulk and trace elements in one run of analysis. For instance, the good correlation between the phosphorus distribution measured by LA-ICP-MS and the oxygen distribution acquired by LIBS, along with a suitable biological interpretation for this finding highlights the value of multimodal analysis approaches. This example outlines the fact that the simultaneous use of LA-ICP-MS and LIBS can be beneficial—especially when the stand-alone techniques cannot detect all the elements of interest.

References

- (1) J.S. Becker, *Methods Mol. Biol.* **656**, 51–82 (2010).
- (2) I. Konz, B. Fernandez, M.L. Fernandez, R. Pereiro, and A. Sanz-Medel, *Anal. Bioanal. Chem.* **403**(8), 2113–25 (2012).
- (3) R. Russo, *Talanta* **57**(3), 425–51 (2002).
- (4) J. Lear, D.J. Hare, F. Fryer, P.A. Adlard, D.I. Finkelstein, and P.A. Doble, *Anal. Chem.* **84**(15), 6707–14 (2012).
- (5) J.S. Becker et al., *Anal. Chem.* **82**(22), 9528–33 (2010).
- (6) M. Bonta, H. Lohninger, V. Laszlo, B. Hegedus, and A. Limbeck, *J. Anal. At. Spectrom.* **29**(11), 2159–67 (2014).
- (7) S. Theiner et al., *Metallomics: Integrated Bio-metal Science* **7**(8), 1256–64 (2015).
- (8) D. Hare, C. Austin, and P. Doble, *The Analyst* **137**(7), 1527–37 (2012).
- (9) A. Limbeck, P. Galler, M. Bonta, G. Bauer, W. Nischkauer, and F. Vanhaecke, *Anal. Bioanal. Chem.* **407**(22), 6593–617 (2015).
- (10) C. Giesen et al., *Nat. Meth.* **11**(4), 417–22 (2014).
- (11) S.J. Van Malderen, E. Vergucht, M. De Rijcke, C. Janssen, L. Vincze, and F. Vanhaecke, *Anal. Chem.* **88**(11), 5783–9 (2016).

- (12) H.A.O. Wang et al., *Anal. Chem.* **85**(21), 10107–10116 (2013).
- (13) S.J.M. Van Malderen, J.T. Van Elteren, and F. Vanhaecke, *J. Anal. At. Spectrom.* **30**(1), 119–25 (2015).
- (14) V. Motto-Ros et al., *Spectrochim. Acta, Part B* **87**, 168–74 (2013).
- (15) L. Sancey et al., *Sci. Rep.* **4**, article number: 6065 (2014).
- (16) M. Dong et al., *Spectrochim. Acta, Part B* **109**, 44–50 (2015).
- (17) K. Subedi, T. Trejos, and J. Almirall, *Spectrochim. Acta, Part B* **103–104**, 76–83 (2015).
- (18) J. Bianga et al., *Metallomics: Integrated Bio-metal Science* **6**(8), 1382–6 (2014).
- (19) M. Bonta, J.J. Gonzalez, C. Derrick Quarles, R.E. Russo, B. Hegedus, and A. Limbeck, *J. Anal. At. Spectrom.* **31**(1), 252–8 (2016).
- (20) M. Bonta, H. Lohninger, M. Marchetti-Deschmann, and A. Limbeck, *The Analyst* **139**(6), 1521–31 (2014).
- (21) D.J. Fawthrop, A.R. Boobis, and D.S. Davies, *Arch. Toxicol.* **65**(6), 437–44 (1991).
- (22) J. Durlach, *Magnesium in Clinical Practice* (J. Libbey, London, UK, 1988).
- (23) J.E. Coleman, *Annu. Rev. Biochem.* **61**, 897–946 (1992).

Maximilian Bonta and Andreas Limbeck

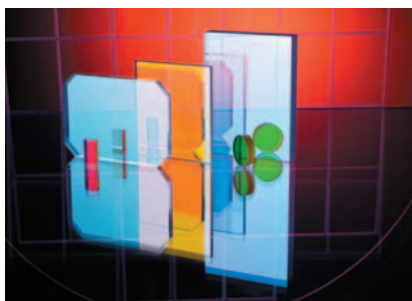
are with TU Wien, Institute of Chemical Technologies and Analytics in Vienna, Austria. **Szilvia Török** is with the Department of Tumor Biology at the National Koranyi Institute of Pulmonology in Budapest, Hungary. **Balazs Döme** is with the Department of Tumor Biology at the National Koranyi Institute of Pulmonology, the Division of Thoracic Surgery, Department of Surgery, Comprehensive Cancer Center at the Medical University of Vienna in Austria, the Department of Biomedical Imaging and Image-guided Therapy, Division of Molecular and Gender Imaging, Medical University of Vienna, and the Department of Thoracic Surgery, Semmelweis University and National Institute of Oncology in Budapest, Hungary. Direct correspondence to: andreas.limbeck@tuwien.ac.at ■

For more information on this topic, please visit our homepage at: www.spectroscopyonline.com

PRODUCTS & RESOURCES

Alluxa Ultra Series Filters

Alluxa Ultra Series Filters, including Narrowband, Dichroic, UV, IR, and Notch filters, provide the highest performance optical thin film solutions available today. For example, the Ultra Series Flat Top Narrowband filters offer the narrowest bandwidths and squarest filter profiles in the industry. They are available in the visible and NIR with FWHMs of 0.25 nm to 2 nm, transmission levels of >90%, and OD6 blocking out of band.



All Alluxa Ultra Series filters are intended to offer OEM customers and researchers higher performance than off-the-shelf products. They highlight Alluxa's commitment to tighter specification tolerances in order to provide the best possible system level performance.

Alluxa Inc.,
Santa Rosa, CA;
www.alluxa.com



FT-NIR system

PerkinElmer's Spectrum Two N transportable FT-NIR system is designed for NIR analysis. According to the company, the system has plug-and-play accessories and is suitable for users with different levels of expertise, including novices and seasoned professionals.

PerkinElmer,
Waltham, MA;
www.perkinelmer.com



NIR spectral sensor kit

The NeoSpectra Micro Development kit from Si-Ware is designed as a plug-and-play product for application with its NeoSpectra Micro, chip-sized, self-contained near-infrared (NIR) spectral sensor. According to the company, the sensor has a spectral range of 1250–2500 nm, and the kit includes the development board with an SPI interface, a Raspberry Pi board, mini HDMI, and a micro USB cable.

Si-Ware Systems, Flintridge, CA; www.neospectra.com



RoHS liquid cells

Spectral Systems' restriction of hazardous substances (RoHS) Super-Sealed liquid cells are designed and manufactured for precision quantitative analysis and reproducibility. According to the company, the cells use fluoropolymer seals to eliminate lead and mercury amalgam.

Spectral Systems,
Hopewell Junction, NY;
www.spectral-systems.com



Wide-range wavelength reference

A certified reference material from Starna reportedly provides 14 well defined, evenly spaced, and interference-free peaks for spectrophotometer wavelength qualification covering a wavelength range of 240–795 nm. According to the company, the reference combines holmium and didymium (neodymium and praseodymium) and covers the most popular wavelengths in UV and visible spectrophotometry.

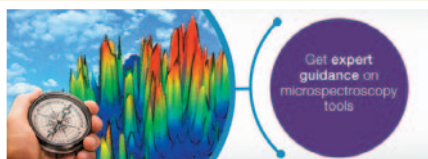
Starna Cells, Inc., Atascadero, CA; www.starna.com



Microspectroscopy selection guide

Thermo Fisher's microspectroscopy guide is designed to provide information about FT-IR and Raman microscopes, and microsampling systems. According to the company, experts are available for advice about IR or Raman microscopy and microsampling systems, and the guide can be downloaded at www.thermofisher.com/microspectroscopy.

Thermo Fisher Scientific, Madison, WI;
www.thermofisher.com



Multispectral imaging camera

The PIXELTEQ brand SpectroCam VIS-SWIR 640 multispectral imaging camera from Ocean Optics is designed for short-wavelength infrared imaging in tissue and biologic material analysis for medical and forensics applications. According to the company, the device has an InGaAs sensor for increased sensitivity, full frame 640 x 512 pixel resolution and 15- μ m pixel pitch, and can produce live processed images of six spectral bands at a rate of up to 25 frames per second.

Ocean Optics,
Dunedin, FL;
www.oceanoptics.com



Modular benchtop lasers for Raman systems

Ondax's BT Series and CleanLine TR Series benchtop lasers are designed for plug-and-play use with laboratory Raman setups. According to the company, the BT Series is offered in both 350-mW and 500-mW versions at 785 nm, 830 nm, 976 nm, and 1064 nm, and The CleanLine TR Series, for low-frequency terahertz Raman applications, is available in 80 mW at 785 nm and 853 nm, as well as 250 mW at 976 nm.

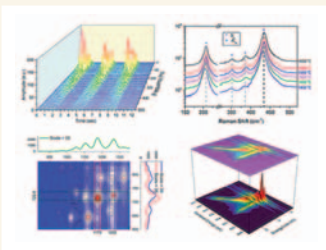
Ondax, Inc.,
Monrovia, CA;
www.ondax.com



Data analysis and graphing software

Origin and OriginPro 2017 data analysis and graphing software from OriginLab reportedly includes more than 100 new features and improvements. According to the company, enhancements include plot menu with large icons, improved graph annotation tool, simplified column calculations, and new apps such as principal component analysis for spectroscopy.

OriginLab,
Northampton, MA;
www.OriginLab.com



Autosampler

The YZ autosampler from PIKE Technologies is designed for sample transmission measurements where precise mapping is required. According to the company, the autosampler's Y and Z plane movement (no rotation) makes it suitable for spectroscopic measurements of samples having a spectral signature influenced by orientation, such as a polarized film.

PIKE Technologies,
Madison, WI;
www.piketech.com



Benchtop XRD system

Rigaku's MiniFlex benchtop X-ray diffraction system is designed for phase identification and quantification, and the determination of percent (%) crystallinity, crystallite size and strain, lattice parameter refinement, Rietveld refinement, and molecular structure. According to the company, the system can be used in research in material science and chemistry, and in industry for research and quality control.

Rigaku Corporation,
Tokyo, Japan;
www.rigaku.com



STATEMENT OF OWNERSHIP, MANAGEMENT, AND CIRCULATION

(Requester Publications Only)
(Required by 39 USC 3685)

1. **Publication Title:** Spectroscopy
2. **Publication Number:** 0887-6703
3. **Filing Date:** 9/30/2017
4. **Issue Frequency:** Monthly
5. **Number of Issues Published Annually:** 12
6. **Annual Subscription Price (if any):** \$79.95
7. **Complete Mailing Address of Known Office of Publication:**
131 West First Street, Duluth, St. Louis County, Minnesota 55802-2065
Contact Person: Wendy Bong
Telephone: 218-740-7244
8. **Complete Mailing Address of Headquarters or General Business Office of Publisher:**
2 Penn Plaza, 15th Floor, New York, NY 10121
9. **Full Names and Complete Mailing Addresses of:**
Publisher: Michael J. Tessalone, 485 F Route 1 South, Suite 210, Iselin, NJ 08830
Editorial Director: Laura Bush, 485 F Route 1 South, Suite 210, Iselin, NJ 08830
Managing Editor: Megan L'Heureux, 485 F Route 1 South, Suite 210, Iselin, NJ 08830
10. **This publication is owned by:** Advanstar Communications Inc., 2 Penn Plaza, 15th Floor, New York, NY 10121. The sole shareholder of Advanstar Communications Inc. is: Rocket Holdings, Inc., 1983 Marcus Ave., Suite 205, Lake Success, NY 11042.
11. **Known Bondholders, Mortgages, and Other Security Holders Owning or Holding 1 Percent or More of Total Amounts of Bonds, Mortgages, or Other Securities. If none, check box** **None**
12. **Does Not Apply**
13. **Publication Title:** Spectroscopy
14. **Issue Date for Circulation Data Below:** August 2017
15. **Extent and Nature of Circulation**

	Average No. Copies Each Issue During Preceding 12 Months	No. Copies of Single Issue Published Nearest to Filing Date
A. Total Number of Copies	18,763	16,764
B. Legitimate Paid and/or Requested Distribution		
1. Outside County Paid/Requested Mail Subscriptions Stated on PS Form 3541	14,418	12,871
2. In-County Paid/Requested Mail Subscriptions Stated on PS Form 3541	0	0
3. Sales Through Dealers and Carriers, Street Vendors, Counter Sales, and Other Paid or Requested Distribution Outside USPS	30	67
4. Requested Copies Distributed by Other Mail Classes Through the USPS	0	0
C. Total Paid and/or Requested Circulation (Sum of 15b (1), (2), (3), and (4))	14,448	12,938
D. Non-requested Distribution		
1. Outside County Non-requested Copies Stated on PS Form 3541	3,849	3,596
2. In-County Non-requested Copies Stated on PS Form 3541	0	0
3. Non-requested Copies Distributed Through the USPS by Other Classes of Mail	0	0
4. Non-requested Copies Distributed Outside the Mail	438	179
E. Total Non-requested Distribution (Sum of 15d (1), (2), (3) and (4))	4,286	3,775
F. Total Distribution (Sum of 15c and e)	18,734	16,713
G. Copies not Distributed	29	51
H. Total (Sum of 15f and g)	18,763	16,764
I. Percent Paid and/or Requested Circulation	77.12%	77.41%

16. Electronic Copy Circulation

*If you are not claiming electronic copies, skip to line 17

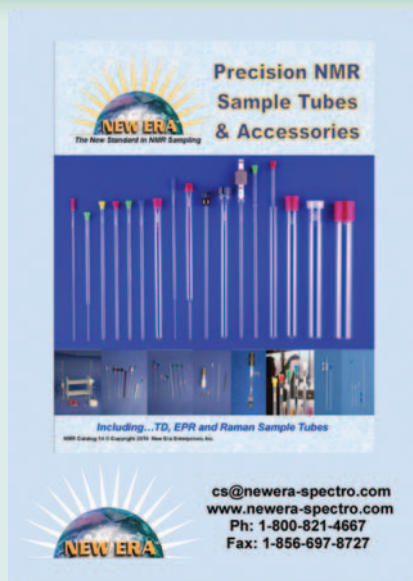
17. Publication of Statement of Ownership for a Requester Publication is required and will be printed in the October issue of this publication.

Name and Title of Editor, Publisher, Business Manager, or Owner:
Christine Shappell, Audience Development Director
Signature:

Christine Shappell

Date: 9/30/17

I certify that the statements made by me above are correct and complete.



Ad Index

ADVERTISER	PG#
ABB, Inc.....	5
Alluxa, Inc.	27
CEM Corporation.....	11
Cobolt AB.....	33
Edinburgh Instruments.....	35
Harrick Scientific Corporation.....	CV3
Hitachi High Technologies America, Inc.....	6
HORIBA Scientific.....	7
Milestone, Inc.	3, 50
MKS Instruments, Inc.....	31
New Era Enterprises, Inc.....	49
Ocean Optics, Inc.	CV2
Ondax.....	29
OriginLab Corporation.....	25
PerkinElmer Corporation.....	CV4
PIKE Technologies.....	19
Rigaku GMG.....	9
Si-Ware Systems.....	6
Spectral Systems.....	4
Starna Cells, Inc.....	4, 39
Thermo Fisher Scientific.....	21, 23



Determination of Heavy Metals in Cannabis Plants with Closed Vessel Microwave Digestion

Eric Farrell, Milestone, Inc.

The Milestone Ethos UP microwave digestion system incorporates all the benefits of closed vessel digestion—speed, data quality, and ease-of-use in a safe and compact bench-top system. Together with our MAXI-44 rotor's high throughput and "vent-and-reseal" technology, it is the ideal solution to meet the demands of both government and private laboratories.

The cannabis industry is currently one of the fastest growing industries in the United States. This growth is fueled by recent revelations in the potential benefits of cannabinoid therapies for various medical conditions. Although systems for growing, production, and sale of cannabis and cannabis related products are well established, regulation and enforcement of quality and safety testing have lagged, such as the testing of heavy metals.

This new era of acceptance and legalization has opened new opportunities for labs. Standardization of these methods for the industry will give regulators the resources they need to adapt sensible requirements for regulation and legislation for the use of cannabis within the United States.

Instrumentation

Milestone's Ethos UP microwave digestion system is a flexible and high performing platform used in trace element and routine analysis in laboratories. The Ethos UP is constructed of 18/8 stainless steel, features a built-in camera and can accommodate both high-pressure and high-throughput rotors. Included are 300 built-in digestion methods, which virtually eliminate any method development. In addition, the Ethos UP features Milestone Connect, which enables remote system control via any computer, tablet, or PC, and access to Milestone's 30 years of experience in sample preparation, 24/7/365.

Our MAXI-44 high throughput rotor accommodates up to 44 vessels and is perfectly suited for digestion of cannabis materials. The MAXI-44 is fully controlled by contactless sensors that directly monitor the temperature and pressure of each vessel. Together with Milestone's patented "vent-and-reseal" technology, maximum safety and digestion quality are assured, while minimizing the loss of volatile elements.

Method Details

Digestions were carried out using Milestone's Ethos UP microwave digestion system with MAXI-44 high throughput rotor. Cannabis flower (0.2 g) was weighed directly into the sample vessel, into which 8 mL of HNO₃ was added.

Microwave Program

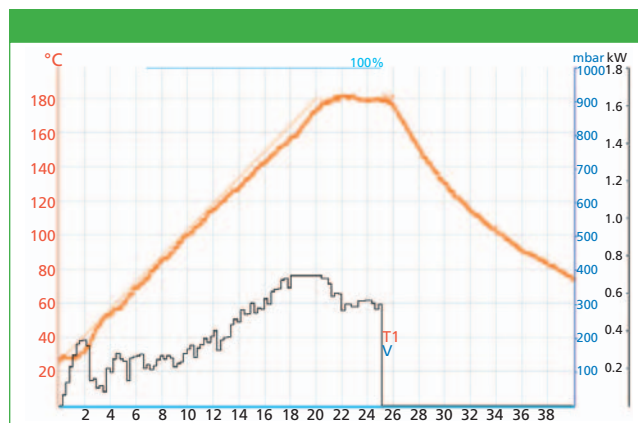


Figure 1: Ethos UP digestion program with 20-min ramp to 180 °C, and a 10-min hold at 180 °C. The line T2 shows the actual temperature achieved. The applied microwave power is automatically controlled by the system so the actual digestion temperature precisely follows the programmed temperature profile.

Table I: Finished product results

	⁷⁵ As			¹¹¹ Cd			²⁰² Hg			²⁰⁸ Pb		
Spike (ppb)	20	80	160	20	80	160	10	40	80	20	80	160
Recovery (%)	114	109	109	98.6	97.5	100	104	107	105	101	101	99.3
	113	113	111	95.8	97.2	99.3	107	101	106	99.2	102	99.3
	108	112	112	96.5	97.1	98.2	103	103	104	102	101	98.7
	110	118	113	97.7	99.2	97.3	107	104	101	101	101	101
	108	115	111	98.0	99.0	97.2	108	104	106	102	103	100
	106	115	114	95.6	100	97.4	106	101	105	103	101	101
Avg. Rec. (%)	110	114	112	97.0	98.3	98.2	106	103	105	101	101	99.9
RSD (%)	2.9	2.7	1.6	1.3	1.2	1.3	1.6	2.1	1.7	1.2	0.6	0.8

Conclusion

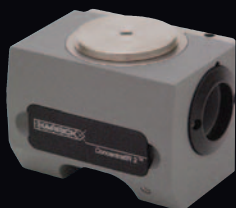
Milestone's ETHOS UP with MAXI-44 high throughput rotor offers multiple benefits for sample preparation in trace metals analyses of cannabis plants and derivatives. The data shown demonstrate the ability of Milestone's Ethos UP to be a highly reproducible and efficient solution, yielding excellent recoveries of As, Cd, Hg, and Pb from cannabis flower.

Milestone, Inc.

25 Controls Drive, Shelton, CT 06484
tel. (866) 995-5100, fax (203) 925-4241
Website: www.milestonesci.com

the
**NEXT
GENERATION**

ConcentratIR2™



A high-precision multiple reflection ATR accessory measuring only 18.5 cubic inches. Designed for microliter sampling. Compact enough to fit any spectrometer.

Choice of diamond or silicon ATR crystals.
Flow and heated options available.



harricksci.com/ConcentratIR2



EXPAND YOUR RANGE EXTEND YOUR RESOURCES

The New Avio 500 ICP-OES - High throughput with low cost of ownership

The Avio® 500 ICP-OES combines the productivity you need with the high-quality performance and faster return on investment your work demands. With high sensitivity and superior resolution, your lab can accomplish more, even when dealing with the most difficult samples. And with the lowest argon consumption of any ICP, simultaneous background correction, and high throughput enabled by Dual View technology, it all comes together to expand the range of what you can accomplish. High throughput. Low cost of ownership. Superior performance. It's everything you want in an ICP-OES system.

For more information, visit perkinelmer.com/avio500



Avio 500 ICP-OES